SAND REPORT
SAND2002-1755
Unlimited Release
Printed June 2002

Amorphous Diamond MEMS and Sensors

John P. Sullivan, Thomas A. Friedmann, Carol I. Ashby, Maarten P. de Boer, W. Kent Schubert, Randy J. Shul, Robert J. Hohlfelder, and David A. LaVan

Prepared by
Sandia National Laboratories
Albuquerque, New Mexico 87185 and Livermore, California 94550

Sandia is a multiprogram laboratory operated by Sandia Corporation, a Lockheed Martin Company, for the United States Department of Energy under Contract DE-AC04-94AL85000.

Sandia National Laboratories

Issued by Sandia National Laboratories, operated for the United States Department of Energy by Sandia Corporation.

Available to DOE and DOE contractors from
U.S. Department of Energy
Office of Scientific and Technical Information
P.O. Box 62
Oak Ridge, TN 37831

Telephone: (865)576-8401
Facsimile: (865)576-5728
E-Mail: reports@adonis.osti.gov
Online ordering: http://www.doe.gov/bridge

Available to the public from
U.S. Department of Commerce
National Technical Information Service
5285 Port Royal Rd
Springfield, VA 22161

Telephone: (800)553-6847
Facsimile: (703)605-6900
E-Mail: orders@ntis.fedworld.gov
Online order: http://www.ntis.gov/ordering.htm

SAND2002-1755
Unlimited Release
Printed June 2002

Amorphous Diamond MEMS and Sensors

John P. Sullivan and Thomas A. Friedmann
Nanostructure and Semiconductor Physics Department

Carol I. Ashby
Microsensors Science and Technology Department

Maarten P. de Boer
Radiation & Reliability Physics Department

W. Kent Schubert and Randy J. Shul
Microdevice Technologies Department

Robert J. Hohlfelder
Simulation Technology Research Department

Sandia National Laboratories
P.O. Box 5800
Albuquerque, NM 87185-1421

David A. LaVan
MIT
Cambridge, MA 02139

Abstract

This report describes a new microsystems technology for the creation of microsensors and microelectromechanical systems (MEMS) using stress-free amorphous diamond (aD) films. Stress-free aD is a new material that has mechanical properties close to that of crystalline diamond, and the material is particularly promising for the development of high sensitivity microsensors and rugged and reliable MEMS. Some of the unique properties of aD include the ability to easily tailor film stress from compressive to slightly tensile, hardness and stiffness 80 - 90% that of crystalline diamond, very high wear resistance, a hydrophobic surface, extreme chemical inertness, chemical compatibility with silicon, controllable electrical conductivity from insulating to conducting, and biocompatibility. A variety of MEMS structures were fabricated from this material and evaluated. These structures included electrostatically-actuated comb drives, micro-tensile test structures, singly- and doubly-clamped beams, and friction and wear test structures. It was found that surface micromachined MEMS could be fabricated in this material easily and that the hydrophobic surface of the film enabled the release of structures

without the need for special drying procedures or the use of applied hydrophobic coatings. Measurements using these structures revealed that aD has a Young's modulus of ~ 650 GPa, a tensile fracture strength of 8 GPa, and a fracture toughness of 8 $MPa \cdot m^{1/2}$. These results suggest that this material may be suitable in applications where stiction or wear is an issue. Flexural plate wave (FPW) microsensors were also fabricated from aD. These devices use membranes of aD as thin as ~ 100 nm. The performance of the aD FPW sensors was evaluated for the detection of volatile organic compounds using ethyl cellulose as the sensor coating. For comparable membrane thicknesses, the aD sensors showed better performance than silicon nitride based sensors. Greater than one order of magnitude increase in chemical sensitivity is expected through the use of ultra-thin aD membranes in the FPW sensor. The discoveries and development of the aD microsystems technology that were made in this project have led to new research projects in the areas of aD bioMEMS and aD radio frequency MEMS.

CONTENTS

1.0 Introduction

This report summarizes work performed under a laboratory directed research and development (LDRD) project on the integration of amorphous diamond (aD) into sensors and micromachines. This project succeeded in creating a new microsystems technology at Sandia for developing MEMS and sensors with unique or improved functionality. The cornerstone of this new technology is the integration of a material that was invented at Sandia National Laboratories (patent no. 6,103,305, issued on August 15, 2000) which is known as "stress relieved amorphous tetrahedrally-bonded carbon" (called amorphous diamond, aD, in this report). Unlike other materials used in micromachines and sensors, this material is a nano-composite of two phases of carbon, a diamond-like phase and a graphite-like phase. This two-phase nature imparts novel properties: the majority phase of diamond-like carbon gives the material its exceptional hardness, stiffness, and strength similar to that of crystalline diamond; and the graphite-like phase controls the material's electrical and optical properties and plays a key role in structural relaxation. We have used this material to create two new technologies. The first is the creation of robust aD micromachines, also known as MEMS (microelectromechanical systems). These are microscopic devices that were first widely proposed by Richard Feynman in 1959. They are, perhaps, the ultimate limit of miniaturization of the machines that are familiar to us in our macroscopic world, including electrostatic motors, gears, shutters, and switches. The second technology is the creation of amorphous diamond sensors. These sensors employ a very thin aD window or membrane, as thin as a few hundred atomic layers. This thin membrane is sensitive to vibrations, and by suitable sensor construction can be used to detect the presence of specific chemicals or even to sense the environment, such as barometric pressure, temperature, etc.

2.0 Project Objectives

The goals of the LDRD project were to create new high performance chemical sensors and MEMS based on aD and then to use these structures to gain understanding about the unique properties of this material. Activities performed in this project included the demonstration of aD flexural plate wave (FPW) chemical sensors; design and fabrication of electrostatically-actuated and non-actuated MEMS structures; assessment of the chemical sensing ability of the aD sensors; design and demonstration of more complex, multi-level aD MEMS devices; use of aD MEMS structures to evaluate mechanical properties; and development of new understanding of the atomic structure and structural relaxation in aD through the use of new experimental tools.

aD is particularly attractive for MEMS as it provides one solution for eliminating stiction in MEMS and for realizing MEMS with extreme wear resistance (long lifetime), due to its inherent hydrophobicity and excellent tribological properties. To evaluate these properties, several MEMS structures were designed and fabricated, including large electrostatically-actuated comb drives, singly-clamped beam adhesion test structures, and friction-and-wear test structures. Several other MEMS structures were designed, fabricated, and tested in order to evaluate the material's tensile strength and fracture toughness, including a variety of micro-tensile test structures. Research performed in this project identified that the material exhibits a high elastic modulus (close to that of crystalline diamond) and is inert to most chemicals. This has led to new applications in the areas of radio-frequency (rf) mechanical resonators and bioMEMS.

The attraction of aD for use in micro-sensors rests with its high tensile strength and controllable stress, which enables thin membranes to be fabricated. Thin membranes are desirable in order to enhance the chemical sensitivity of FPW sensors. A further benefit is the chemical resistance of the material which makes the sensor suitable for use in aggressive chemical environments and which simplifies the fabrication of sensors using a deep-reactive-ion etch process. In this project, aD FPW chemical sensors were fabricated and tested and knowledge gained from the successful development of these sensors was applied to the development of prototype acoustic sensors.

An important aspect of the research on this project was to use the MEMS and sensor structures and new experimental capabilities to improve the understanding of the atomic structure and structural relaxation behavior of aD. MEMS and membrane structures were used to measure the material's residual stress, strain gradient, Young's modulus, tensile fracture strength, fracture toughness, in-plane electrical conductivity, and adhesion energy. Temperature-dependent conductivity, ^{13}C solid-state nuclear magnetic resonance (NMR), and fluctuation electron microscopy measurements were performed to understand the nature of the ordering of the two types of carbon in this material and how the carbon bonding changes with thermal annealing. Insight was gained into the nature of the structural and stress relaxation of this material, reinforcing that this material exhibits novel properties particularly when compared to conventional amorphous covalently-bonded solids, such as amorphous Si or amorphous Ge.

3.0 Amorphous Diamond: Structure, Deposition, and Properties

3.1. Atomic Structure

Amorphous diamond is a pure carbon material in which a majority of carbon atoms are 4-fold coordinated with sp^3-like bonding between atoms (as is found in crystalline diamond), and a minority of carbon atoms are 3-fold coordinated with sp^2-like bonding (as is found in crystalline graphite). Most theoretical models for this material indicate that the 3-fold coordinated atoms form low-dimensional (chain-like) clusters embedded in the 4-fold carbon matrix [1]; hence, the material can be thought of as a two-phase mixture or a nanocomposite. One of the theoretical models for this material which was calculated by Schultz *et al.* is shown in Fig. 3.1 [2]. In the model, the 4-fold coordinated carbon atoms (shown in gray) account for ~ 70% of the atoms with the remainder being 3-fold coordinated (in blue).

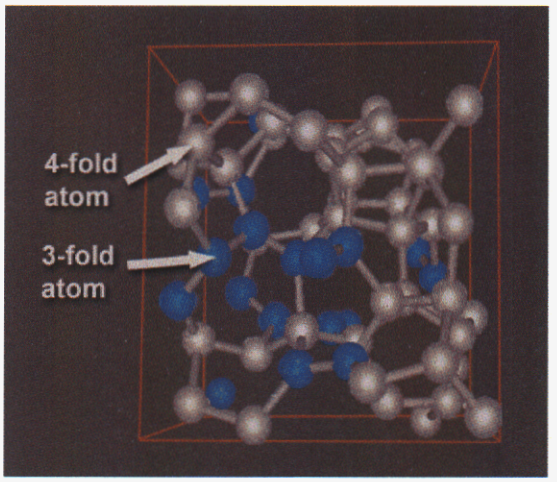

Fig. 3.1. Structure of aD as calculated by Schultz et al.

3.2. Deposition of aD

aD is deposited at room temperature using an energetic pure carbon beam that contains a significant fraction of carbon ions with energies peaked near 100 eV. In this work, the aD films were deposited using pulsed-laser deposition (PLD) with a KrF excimer laser source (248 nm) and a rotating solid graphite target [3]. Alternative methods exist for producing aD, the most common being filtered cathodic arc deposition or mass-selected ion deposition. The films produced by these techniques are referred to as tetrahedrally-coordinated amorphous carbon (ta-C), but they are structurally very similar to aD. One important difference is that stress relaxation in ta-C films seems to not be well-controlled, as compared to aD. This results in the disadvantage that it is difficult to produce low stress films in ta-C (which is an important point for fabricating MEMS and sensors).

For both the fabrication of MEMS and sensors, the laser fluence for PLD was 100 J/cm^2 (pulse width ~ 10 nsec, 20 Hz rep-rate), and the deposition chamber pressure was less than 10^{-7} Torr. For MEMS, the films were deposited on SiO_2-coated (2 μm thick) Si substrates to a thickness of 1 to 2 μm. In most cases, a thin adhesion layer of poly-Si (~ 0.1 μm thick) was used between the SiO_2 layer and aD. Typical deposition rates used in this study were about 1 μm in 3 hours, with uniform thickness (< 10% variation) over a 2" diameter area. (For commercial applications of aD, it would be most efficient to use a filtered carbon cathodic arc source. These systems can produce deposition rates exceeding 2 μm/hr on 4" diameter substrates.) For the relief of residual film stress, the films were annealed in vacuum or inert gas (Ar). Typical annealing conditions were 600 – 650°C for ~ 5 min. or 550°C for more than one hour (when precise control of residual film stress was required). The deposition of films for sensors was similar, except the films were typically deposited directly on Si wafers and the film thickness was typically thinner, as thin as 80 nm.

3.3. Structural Relaxation

As-deposited, aD films are under a state of biaxial film stress (in the film plane) of up to 8 GPa compressive. This extremely high value of stress, which is significantly higher than the ~ 4.5 GPa of hydrostatic stress that is needed to convert graphite into crystalline diamond at high

temperatures, is unacceptable for the creation of MEMS and sensors. Generally, a prospective MEMS material should exhibit a residual stress less than 10 MPa, ideally just a few MPa. For a high modulus material this is an extreme requirement, e.g. for aD this stress level corresponds to an elastic residual strain of about 0.00001 (or about 1 Å of displacement for every 10 μm of beam length, assuming uniaxial loading). Remarkably, properly prepared aD films can exhibit complete stress relaxation to a residual stress level down to zero or even to slightly tensile values, if desired [4]. This stress relaxation is achieved through thermal annealing at modest temperatures, typically less than 650°C (see Fig. 3.2).

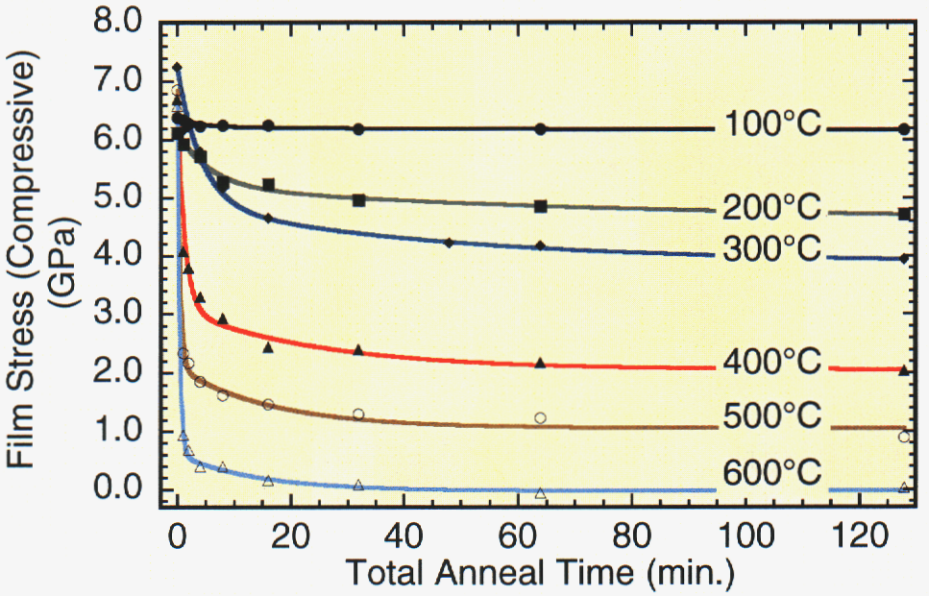

Fig. 3.2. Reduction in compressive film stress in aD with time-temperature annealing in an inert environment (Ar).

The mechanism of stress relaxation in aD is unconventional. The temperature of stress relaxation is inconsistent with viscous flow or creep which would require long-range diffusional motion. The relaxation itself is also irreversible: after annealing to 600°C, for example, there is negligible change in stress upon annealing at lower temperatures, e.g. 400° or 500°C, unless the subsequent annealing time is very much longer than the original anneal time. In an effort to understand the nature of stress relaxation in this material, the temperature-induced structural changes that occur in this material has been studied.

One conventional approach to studying local structure in amorphous materials is the use of radial distribution or pair-correlation functions, G(r). This function describes the probability that there will be two atoms that are separated by a distance, r. The radial distribution function is determined from x-ray or electron diffraction from the amorphous film. Fig. 3.3. shows the measured radial distribution function that was obtained from an as-deposited aD film of high stress as well as the radial distribution function from a separate area of the same film that had been annealed at 600°C in order to relieve the film stress [5]. These measurements were taken through the use of transmission electron diffraction on aD films < 100 nm thick. As shown in the Figure, there is very little *apparent* change in local order that results from the thermal annealing.

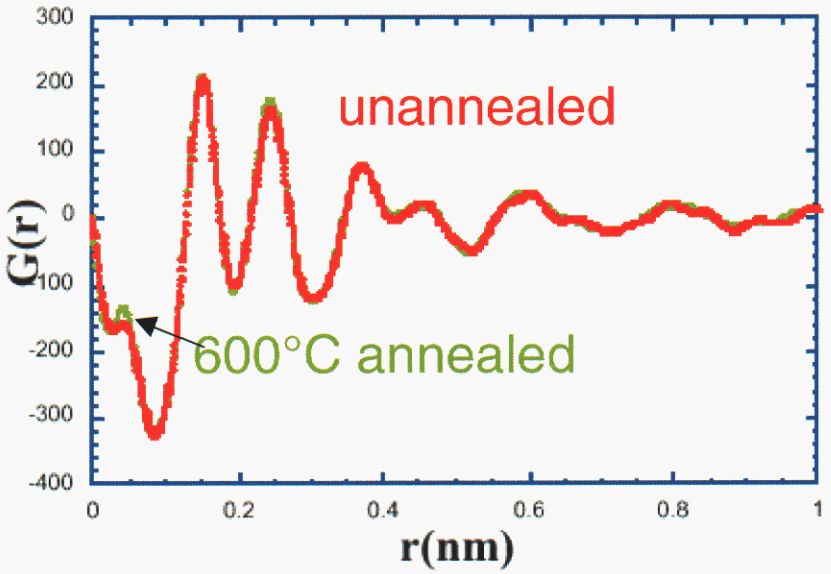

Fig. 3.3. Radial distribution function for annealed and unannealed aD.

Recently, an improved electron microscopy technique has been developed to quantify medium range ordering in amorphous materials [6]. This technique, known as variable coherence microscopy or fluctuation microscopy, samples higher order correlation functions – up to the 4-body correlation function – and is especially sensitive to medium range order. The experiment involves measurement of the maximum variance in dark-field image intensity (i.e. magnitude of the fluctuations in image contrast) as a function of the coherence length of the electron source. The coherence of the electron source is varied by adjusting the inner semiangle of a hollow cone electron illumination source (this can be achieved by applying sine and cosine signals to the x and y illumination deflection coils that position the electron beam).

Fluctuation microscopy was performed on an aD film from which specimens were taken and annealed in vacuum at temperatures ranging from 200°C up to 1000°C. The variance-coherence plot is shown in Fig. 3.4. Several conclusions can be drawn from the plot: (1) The peaks near 5 nm^{-1} and 8.5 nm^{-1} for all samples indicate the presence of significant medium range ordering. (An ideal continuous random network would not show any peaks in the variance-fluctuation plot.) (2) The amount of ordered material or the degree of order increases with annealing, as revealed by the increase in peak height (although the amount of order does not appear to increase monotonically for the peak at 8.5 nm^{-1}). This observed increase in order is contrary to what has been observed for a-Ge and a-Si [6] which show a decrease in order with annealing (below the crystallization temperature), eventually becoming close to a true continuous random network. This difference further emphasizes the unique behavior of a-C when compared to other amorphous Group IV materials. (3) After the 1000°C anneal, there is a pronounced peak at ~ 3 nm^{-1}. This value is very close to the reciprocal lattice spacing of the interlayer spacing of graphite or glassy carbon materials and strongly suggests that the appearance of this peak is associated with the onset of graphite sheet-like ordering in the material. In support of this conclusion, independent measurements using Raman spectroscopy have indicated that aD exhibits a structure similar to glassy carbon (disordered graphite sheets) following annealing at temperatures > 900°C [7]. The absence of this peak in samples annealed at lower temperatures

suggests that sheet-like ordering is not present in any significant extent in aD annealed up to 600°C.

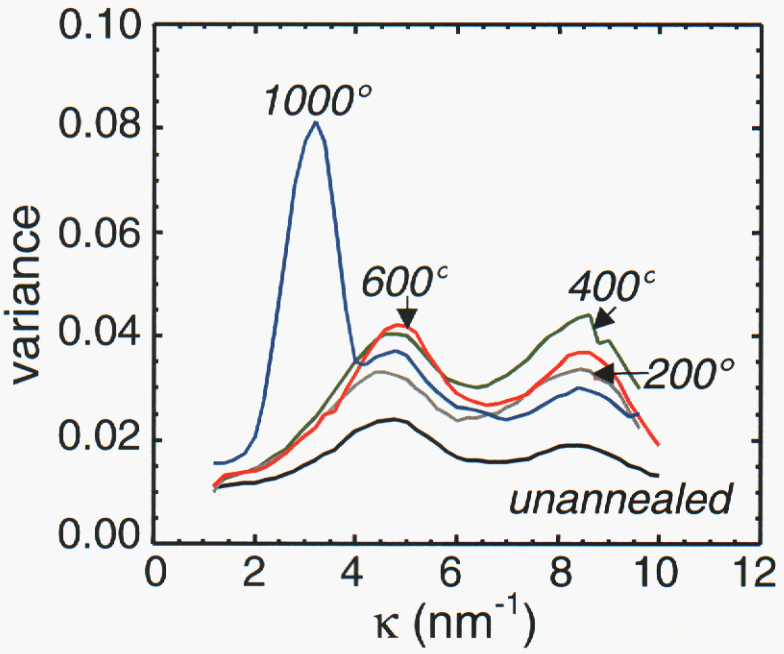

Fig. 3.4. Variance-coherence plot showing the increase in medium range order in aD with annealing.

Further evidence of the structural changes that occur with annealing is revealed by electrical measurements of aD films. aD is often considered to be a wide band gap semiconductor, but its electrical properties are closer to that of a "dirty insulator" (a material with a wide gap, but with a significant density of electronic states within the gap) [8]. Schematically, the density of electronic states in aD is dominated by bands of σ-derived states that are associated with the sp^3 and sp^2 bonded regions of the material. The gap between the occupied and unoccupied σ-bands is about 5.5 eV, i.e. the band gap of crystalline diamond. Between the σ-bands lies π-bands that are associated with the delocalized π-states from the 3-fold coordinated carbon atoms. These π-states have tails that extend throughout the gap created by the σ-bands, see Fig. 3.5.

Electronic conduction in this material is due primarily to electron tunneling between localized π -states, i.e. hopping conduction. The conductance, G_{ij}, between localized states, i and j, has the functional form, $G_{ij} \approx \frac{e^2}{k_B T} \nu_0 \exp(-2\alpha R_{ij}) \exp(-\Delta E_{ij} / k_B T)$, where ν_0 is an attempt frequency, α^{-1} is proportional to the spatial extent of the wavefunction localized to the tunneling state, R_{ij} is the distance between tunneling states, and ΔE_{ij} is the difference in energy between states.

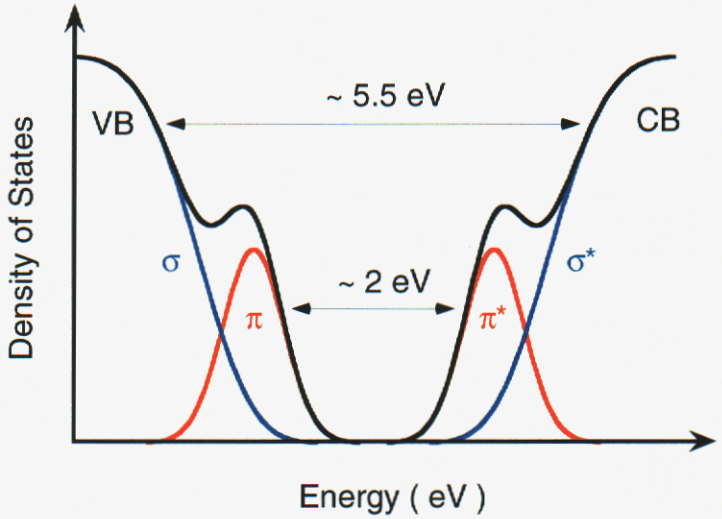

Fig. 3.5. Schematic density of states for aD. The σ-derived bands form the primary band edges. π-bonded states occupy the band gap and are responsible for most of the electrical conductivity.

Thermal annealing results in an interesting effect on electronic conduction in aD. The electrical conductivity of the material increases, and this increase is due to a decrease in the activation energy for tunneling (i.e. G_{ij} increases due to a decrease in ΔE_{ij}, not due to a decrease in R_{ij}), see Fig. 3.6. We attribute this decrease in ΔE_{ij} to an increase in size of the 3-fold low-dimensional clusters $\Rightarrow$ chain ripening. Chain ripening leads to a decrease in the energy gap between occupied and unoccupied π-states on the 3-fold cluster. For example, Robertson has shown theoretically that for isolated π-bonded chains the gap between occupied and unoccupied levels, $E_{\pi-\pi^*}$, is approximately given by 18 eV / N, where N is the number of carbon atoms in the chain [9]. Increasing the number of carbon atoms in a small cluster from 10 to 12 would decrease the gap by 0.3 eV. Ripening of all clusters in the solid has the effect of decreasing the separation between energy levels on neighboring 3-fold clusters, which would lower the requisite activation energy for tunneling. From these measurements we can conclude that one of the effects of annealing aD is to increase the size of the 3-fold coordinated clusters. Little can be said about changes in the 4-fold component of the film on the basis of electrical measurements alone, however. To answer this question, nuclear magnetic resonance (NMR) is required.

Our recent experiments using solid-state NMR on near fully ^{13}C-enriched aD have been very fruitful at identifying the effect of annealing on *both* 4-fold and 3-fold coordinated carbon (the high level of enrichment in ^{13}C is necessary in order to obtain sufficient signal from thin aD films). The chemical shift for 4-fold coordinated carbon is clearly resolved from 3-fold coordinated carbon, enabling easy identification of the ratio of 4-fold to 3-fold carbon, see Fig. 3.7. Annealing leads to a decrease in linewidth for both types of carbon, indicating increasing order throughout the film. This increasing order could, for example, be manifested as a decrease in the range of bond-lengths found in the sample. Furthermore, it is found that annealing for a few minutes does not produce a statistically significant increase in the amount of 3-fold carbon (see Fig. 3.8), which indicates that the ordering is more likely associated with redistribution of existing 4-fold and 3-fold carbon rather than with a conversion between the two types of carbon.

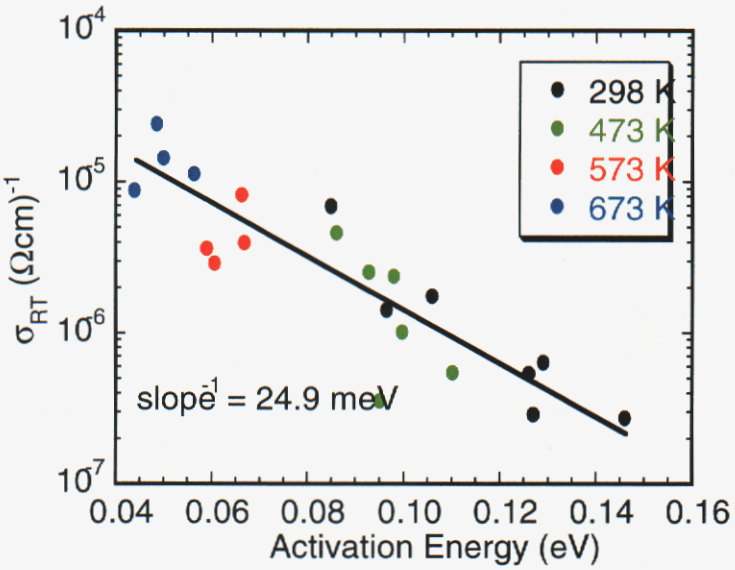

Fig. 3.6. The measured activation energy for electrical transport in aD drops with increasing anneal temperature. This drop in activation energy is sufficient to account for all of the increase in electrical conductivity in this material with annealing. This implies that the tunneling distance is not changing between hopping sites, only the activation energy is changing.

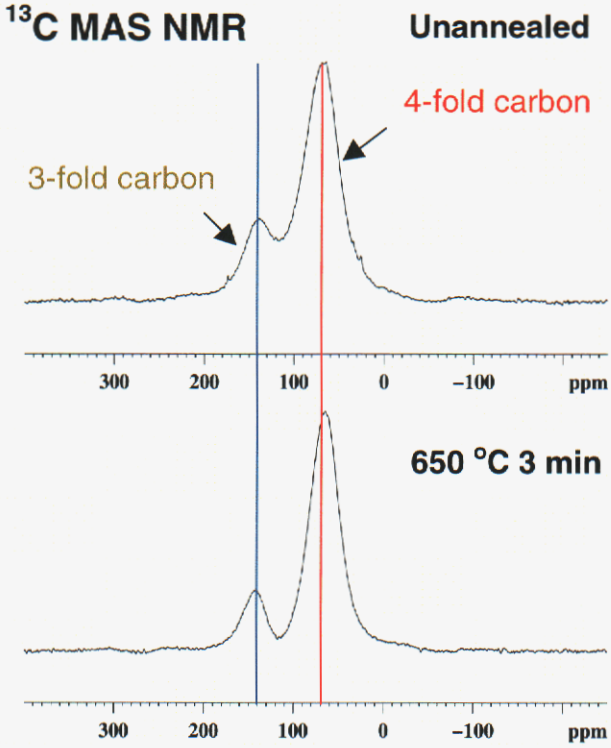

Fig. 3.7. ^{13}C NMR of an unannealed and annealed aD film. Annealing leads to an increase in ordering for both 3-fold and 4-fold coordinated carbon, as evidenced by a decrease in peak line-width.

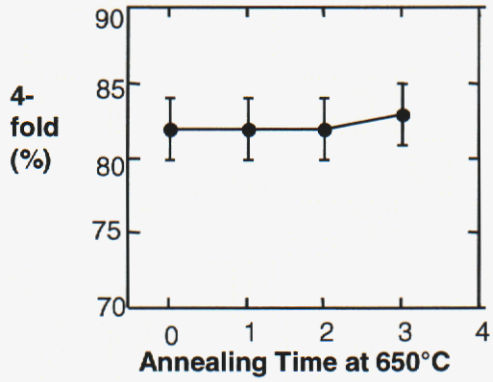

Fig. 3.8. Percentage of 4-fold carbon in an aD film following annealing. There is no statistically significant increase or decrease in 4-fold content with annealing at 650 °C.

A model has been developed to explain the unique form of stress relaxation in aD. The main assumption of the model is that thermal annealing results in rearrangement of the 4-fold and 3-fold network to produce local strain relief within the plane of the film. Consider one specific example of a strain-relieving bond rearrangement, shown schematically in Fig. 3.9. In this example, strain relief in the film plane is achieved by re-orientation of a 3-fold coordinated carbon atom (plus adjustment of the surrounding atoms) so that the short sp^2-bonds are in the plane of the film and the π-bond is normal to the film plane. This particular type of rearrangement would produce a net reduction in the local in-plane strain of ~ 0.29. If only 1-2% of the carbon atoms underwent this type of reorientation, full stress relief (from ~7 GPa to 0 GPa) would be achieved.

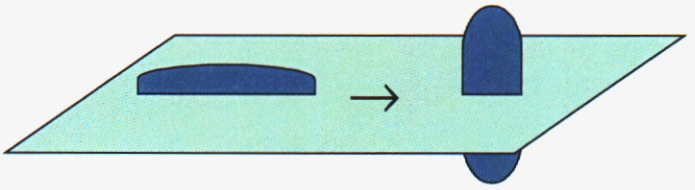

Fig. 3.9. Schematic of one possible strain-relieving bond reorientation in aD. In this example, the bonds associated with a 3-fold carbon atom reorient so that the short sp^2 bonds are in the film plane.

Part of the driving force for this form of bond re-orientation is a reduction in strain energy = $\int \sigma \varepsilon dV$. For a biaxial compressive film stress of 7 GPa, the reduction in strain energy by this type of bond reorientation would be 70 meV/atom, which is substantial. If we assume that the bond reorientation process follows first-order reaction kinetics with an activation energy, E_A, then we can model the kinetics of the stress relaxation as follows

$$\sigma(t,T) = \sigma_0 + \varepsilon_{in-plane} \frac{E}{1-\nu} \int_0^\infty N(E_A)\{1 - \exp[-\nu_0 t \exp(-E_A / k_B T)]\} dE_A, \qquad (1)$$

where σ_0 is the as-deposited film stress, $\varepsilon_{in\text{-}plane}$ is the bond strain relief resulting from bond reorientation, $E/(1-\nu)$ is the biaxial modulus, $N(E_A)$ is the distribution of activation energies, E_A, for the first-order chemical reaction that describes bond reorientaion, and $\nu_0 \exp(-E_A/k_B T)$ is the rate constant for this reaction. The success this model has in describing the experimental data is indicated by the solid lines in Fig. 3.2.

Full stress relief can be achieved after annealing for several minutes at ~ 650°C (or, equivalently, for a few hours at 550°C). This stress relief is accompanied by reorientation of probably just a few % of the carbon bonds, and this small change has almost negligible effect on the film's mechanical properties (hardness and modulus) [3].

One important aspect of this stress relaxation process is that it is irreversible: once the 4-fold carbon bonds with low activation energy convert following annealing, they are no longer available for future stress relaxation (a higher anneal temperature or longer time anneal would be required to access higher activation energy sites). This property is desirable as it enables structural relaxation to occur after annealing at elevated temperature, but essentially zero stress relaxation (in any meaningful time scale) would later occur in the material after cooling back down to room temperature.

3.4 Properties of aD

aD exhibits a suite of properties unique from other materials. Some of these properties include hardness of 90 GPa (10 on the Mohs scale), a Young's modulus of 650 – 700 GPa, a tensile fracture strength of 8 GPa, fracture toughness of 8 $MPa \cdot m^{1/2}$, a coefficient of friction of about 0.1, a refractive index of 2.4, tunable resistivity from 0.1 Ωcm to 10^7 Ωcm, and inertness to almost all chemicals. A summary of the properties of aD that we have measured or, in some cases, estimated are listed in Appendix I.

4.0 Amorphous Diamond MEMS

4.1 Background on Diamond and Amorphous Carbon MEMS

The designer of microelectromechanical systems (MEMS) can increase MEMS performance either by improved mechanical design or by the selection of a MEMS material with improved mechanical performance. In the quest to identify high performance MEMS materials, diamond and amorphous carbon have recently emerged as one promising class of materials. These materials offer excellent tribological properties, low-stiction (hydrophobic) surfaces, chemical inertness, and high elastic modulus. The primary challenge with these materials lies not with improving the materials performance, but rather in integrating their relatively immature deposition processes with the mature, well-established processes derived from the silicon microelectronics industry.

Diamond has the highest hardness (~ 100 GPa) and elastic modulus (~ 1100 GPa) of all materials, see Fig. 4.1. Amorphous forms of carbon, specifically the hard carbons, amorphous diamond (aD), tetrahedral amorphous carbon (ta-C), and diamond-like carbon (DLC), can also approach crystalline diamond in hardness (up to ~ 90 GPa) and modulus (~ 800 GPa). The main appeal of these materials for the MEMS designer, however, lies with their extreme wear resistance (up to 10,000 times greater wear resistance than Si)[1], their hydrophobic surfaces that offer inherent stiction resistance (parts don't stick together due to capillary forces from entrapped water) [2], and their chemical inertness (allows use in aggressive chemical environments). Recently, researchers have made considerable progress in the fabrication of MEMS structures from these materials, both in the area of surface micromachining and in mold-based processes [3]-[10].

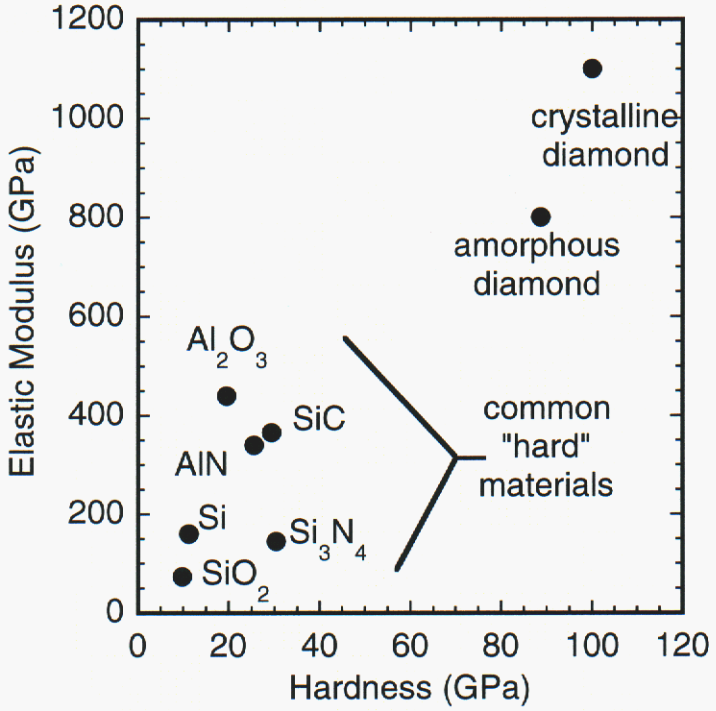

Fig. 4.1. The hardness and elastic modulus of a variety of "hard" materials.

4.2 Nanocrystalline and Polycrystalline Diamond MEMS

Crystalline diamond films having the least amount of long range order are known as ultra-nanocrystalline diamond (UNCD) films [19]. This material is deposited using microwave plasma chemical vapor deposition (CVD) with carbon-60 or methane as the carbon source (the balance being 98% Ar, 1-2% H_2). Structurally, the material is similar to poly-crystalline diamond, but the grain size is 3 to 5 nm, as opposed to ~1 μm typical for conventional poly-crystalline diamond films. This material can be patterned using surface micromachining or used to coat silicon or metal molds which can be subsequently chemically etched away to produce UNCD channels and pipes, including very thin wall structures, see Fig. 4.2.

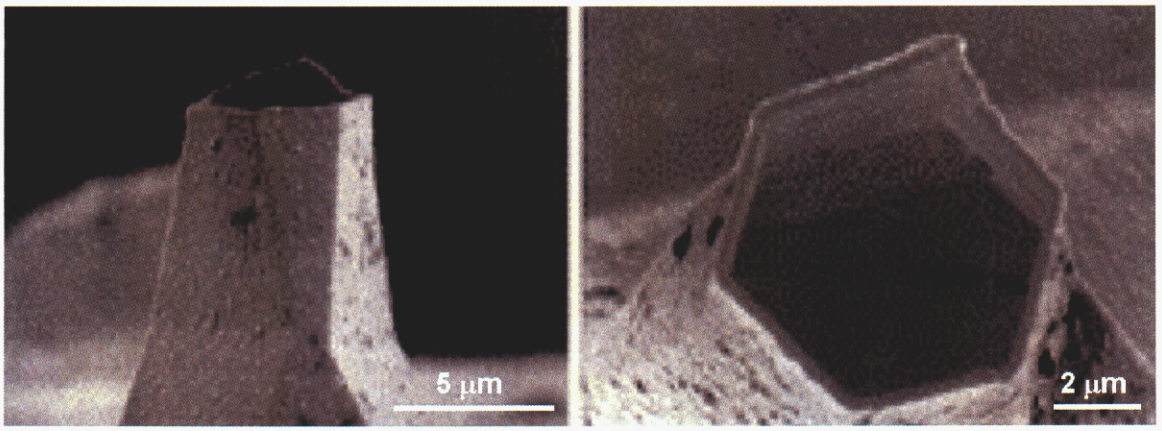

Fig. 4.2. A thin wall tube of ultra-nanocrystalline diamond fabricated by a Si mold and etch process.

Further increases in crystallinity produces true polycrystalline diamond, which has the advantage of retaining the high thermal conductivity of diamond (not found in the less-ordered carbon phases) and good optical transparency (diamond has the widest electromagnetic radiation transparency range of all materials known, ranging from UV to far IR). Several techniques exist for polycrystalline diamond synthesis, including hot flame CVD, microwave plasma CVD, and hot flame (combustion) decomposition, with a typical deposition rate of 1 to 2 μm/hr over a 4" substrate. Despite gem-quality diamond's almost mythical rarity, polycrystalline diamond films can be deposited at lower cost than even low-pressure CVD poly-Si.

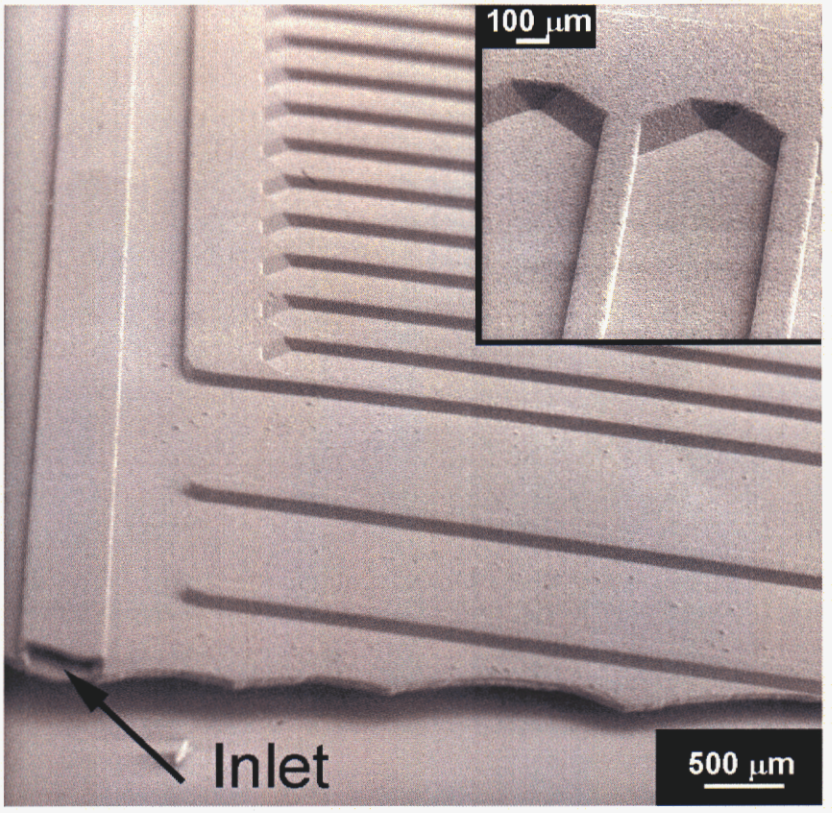

Fig. 4.3. A polycrystalline diamond active cooling device. The inset shows detail of the cooling channels.

The CVD synthesis technique for diamond makes it possible to transfer the properties of diamond to large areas and complicated shapes and forms. Examples of microstructures in polycrystalline diamond include acceleration sensors [15], thermally-actuated liquid ejectors [15], electrical microswitches [16], micro-tweezers [17], high efficiency electron emission microtips [20], diamond cantilevers with tips for scanning probe microscopy (SPM) applications [17],[21], a diamond motor structure [22], diamond gears [23],[24], nanoindentation tips [25], and diamond burrs [26]. In most cases when diamond microstructures are made, the structures need to be supported by a carrier structure of e.g. silicon. In a few cases, completely free-standing diamond microstructures have been demonstrated, and these are particularly useful for optical or thermal management applications, such as laser-to-fiber alignment structures [13],[27], molds for polymer replication [13], and free-standing capillaries [13]. By using silicon-on-insulator (SOI) substrates and a Si-molding approach, precise diamond mechanical structures

may be achieved. Two examples are shown in Figs. 4.3 and 4.4. The first is a polycrystalline diamond active cooling device that takes advantage of diamond's high thermal conductivity, and the second is a diamond fresnel lens for applications in high power diffractive optics [14].

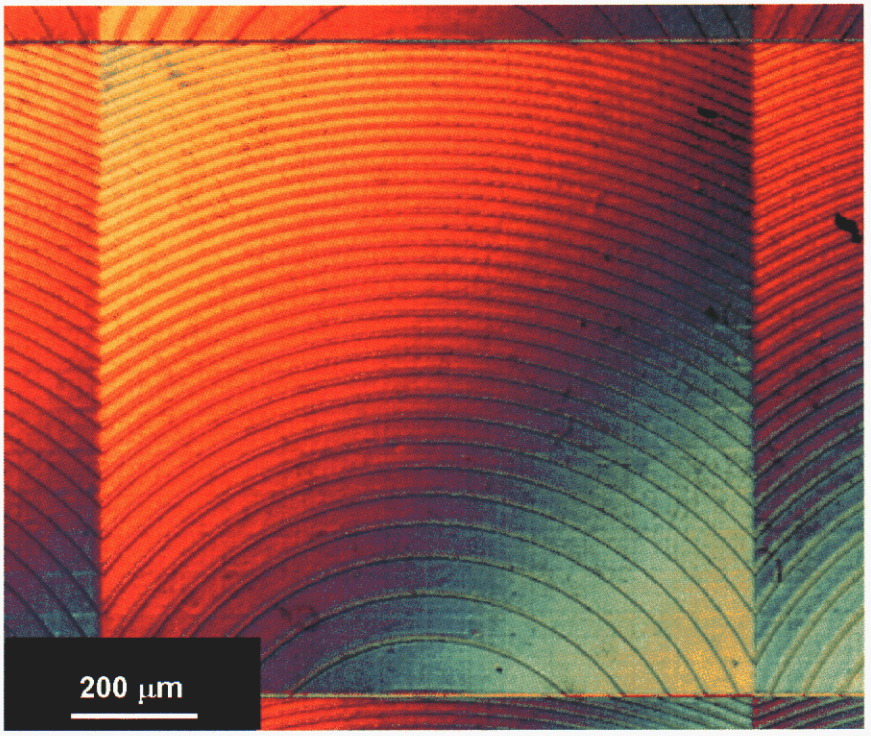

Fig. 4.4 A polycrystalline diamond diffractive optic device.

Lastly, when the high hardness and modulus of diamond or hard carbon is not needed, carbon MEMS structures can be fabricated using soft-lithography approaches (e.g. molds, stampings, impressions, etc.). In this case, the carbon source originates from a liquid-based pre-cursor (an organic liquid or low viscosity polymerizable fluid) that fills a stamped or cast mold. Carbonization of the organic forms glassy carbon (a disordered purely three-fold coordinated carbon material) that possesses mechanical properties similar to that of graphite [28].

Carbon, with its remarkable diversity of structure and exceptional materials properties, shows considerable potential for future MEMS devices. While much progress has been made, challenges remain for integrating polycrystalline diamond or glassy carbon into MEMS. In this project, we have introduced a new technology for integrating carbon into MEMS, viz. amorphous diamond MEMS.

4.3 Fabrication of aD MEMS

Amorphous diamond is a new material for surface-micromachined MEMS that offers promise for reducing wear and stiction of MEMS components. The material is distinguished from crystalline diamond by the fact that it consists of an amorphous mixture of 4-fold and 3-fold coordinated carbon. Due to the high percentage of 4-fold carbon (> 80%), the material has mechanical properties close to that of crystalline diamond. The main advantages of this material over other types of carbon films are that the material can be easily deposited as a thin film from ~ 5 nm thickness to > 5 μm thickness with a surface roughness that is extremely low (~ 0.1 nm

R.M.S.). Also, the stress state of this material can be easily controlled from tensile to compressive. (As described in Chapter 3, a unique form of structural relaxation in this material permits the residual stress to be reduced from an as-deposited value of 8 GPa compressive down to zero stress or slightly tensile values. Irreversible plastic deformation, achieved by heat treating elastically strained structures, is also possible.)

In this project, several types of amorphous diamond MEMS devices have been fabricated, including electrostatically-actuated comb drives, micro-tensile test structures, and cantilever beams. Measurements using these structures have enabled determination of the material's mechanical and physical properties. These include a Young's modulus around 700 GPa, fracture toughness of 8 $MPa \cdot m^{1/2}$, an advancing H_2O contact angle of 84° to 94°, and a surface roughness of 0.1 to 0.9 nm R.M.S. on Si and SiO_2, respectively.

Single-level aD MEMS structures were fabricated by depositing an aD film on to a SiO_2 sacrificial layer on top of Si (the deposition conditions are described in section 3.2). In many cases, a thin layer of poly-Si (0.07 μm) was used between the aD and SiO_2 as an adhesion promoter. The aD film was stress-relieved by thermal annealing to produce zero stress (± 10 MPa stress). Subsequent steps include photolithographically patterning a thin Al layer atop the aD film. The aD layer was then etched in an O_2 electron cyclotron resonance plasma using the patterned Al film as an etch mask. Following dry etching, wet etching of the SiO_2 sacrificial layer was performed using 7:1 H_2O:HF or buffered oxide etch (BOE). Any residual poly-Si on the underside of undercut sections of aD was removed by brief immersion in dilute HF in HNO_3. This process leaves pedestals of SiO_2 supporting completely undercut sections of aD film. Following wet etching, the structures were dried in flowing $N_{2(g)}$, and a brief (5 min.) dehydration bake in Ar at 200 – 300°C was used to remove any residual moisture and free the aD structures from the substrate (unlike poly-Si MEMS, supercritical CO_2 drying or self-assembled monolayer coatings to eliminate auto-adhesion – stiction – were not required). Fig. 4.5 shows the processing sequence, and Appendix II lists design rules for the creation of single-level MEMS.

Control of film stress is one of the most critical issues facing any potential MEMS material, particularly for surface micromachined structures which can have large aspect ratio of the structural elements (beam length/beam thickness can exceed 1000). Generally, a prospective MEMS material should exhibit a residual stress less than 10 MPa, ideally just a few MPa. Equally important is control of stress gradients through the thickness of the material. These stress gradients give rise to out-of-plane distortion of the MEMS structural element and can prevent proper meshing of gears or other, more serious, alignment errors. Ideally, the radius of curvature of a MEMS beam should approach or exceed one meter (this radius of curvature would cause a 100 μm long beam to deflect about 50 Å out of the film plane).

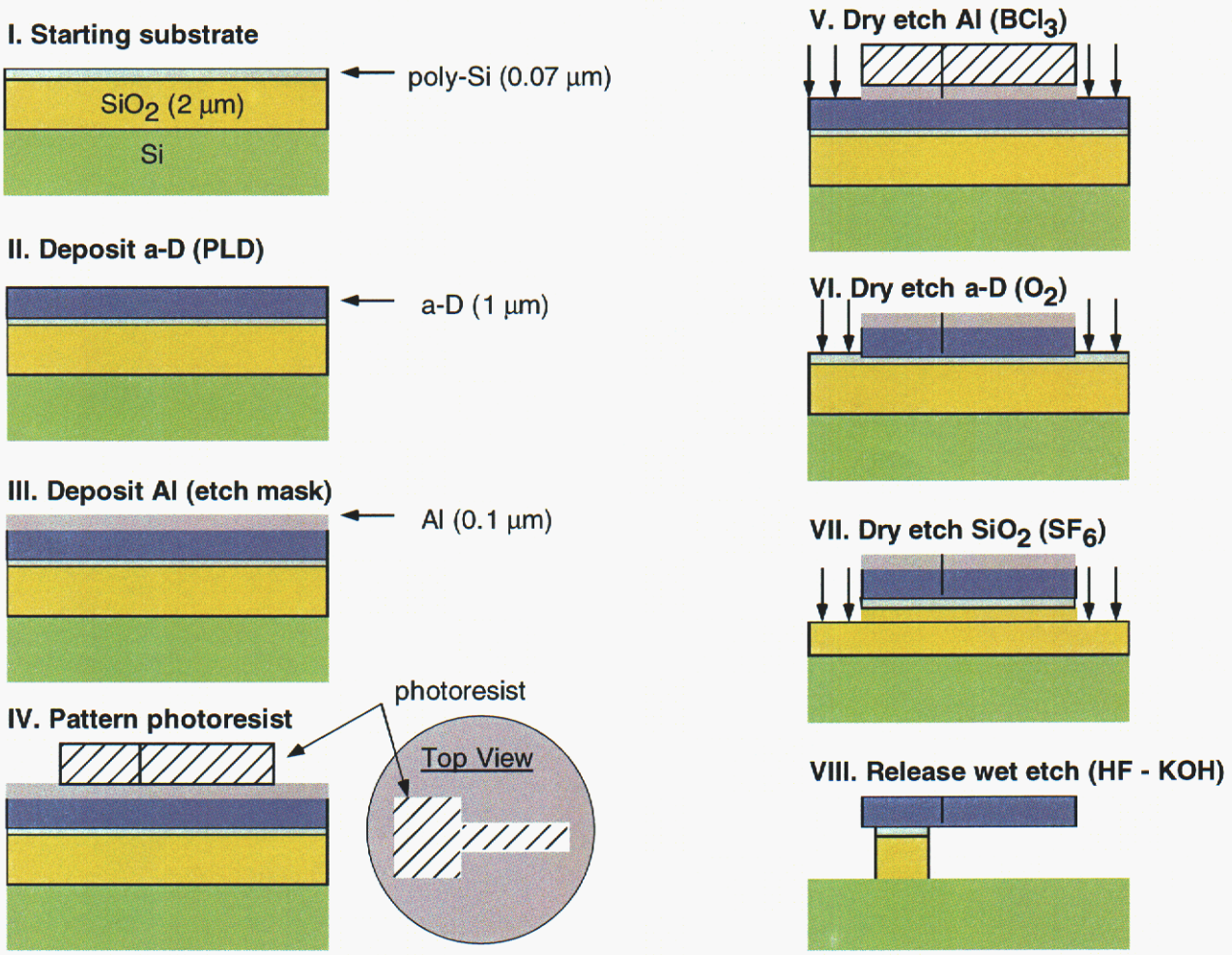

Fig. 4.5. Processing steps to create single-level MEMS structures in aD.

Control of residual film stress in aD permits large aspect ratio MEMS structures. Several examples are shown in figures 4.6-4.8. Figure 4.6 shows an example of an electrostatically-actuated comb drive structure (the inset shows detail of the fingers and spring). This particular structure is used to measure the force that may be generated by the actuator (actuating the structure leads to elliptical distortion of the circular spring in the upper left, and the distortion is measured by a vernier scale in the center). Unlike undoped diamond which is extremely resistive, aD is moderately conductive with a resistivity in its stress-free state of 10^4 Ωcm (the resistivity can be reduced to below 1 Ωcm by higher temperature annealing), and this conductivity is more than sufficient for electrostatic actuation (electronic conduction in this material is due to tunneling between 3-fold coordinated carbon clusters [8]). For unloaded electrostatic comb drives (not shown), a displacement of several μm was observed at a resonance frequency of 5500 Hz and ~ 90 V excitation. The mechanical response of aD comb drives is equivalent to that of poly-Si, except the resonant frequencies are scaled upward by a factor of $(E/\rho)^{1/2}$, where E is the elastic modulus of aD (about 700 GPa, or ~ 5 times higher than poly-Si) and ρ is the density (about 2.9 g/cm^3, or about 26% higher than poly-Si). Therefore, for the same dimensions, the resonant frequency of the aD element is about two times higher than the poly-Si element.

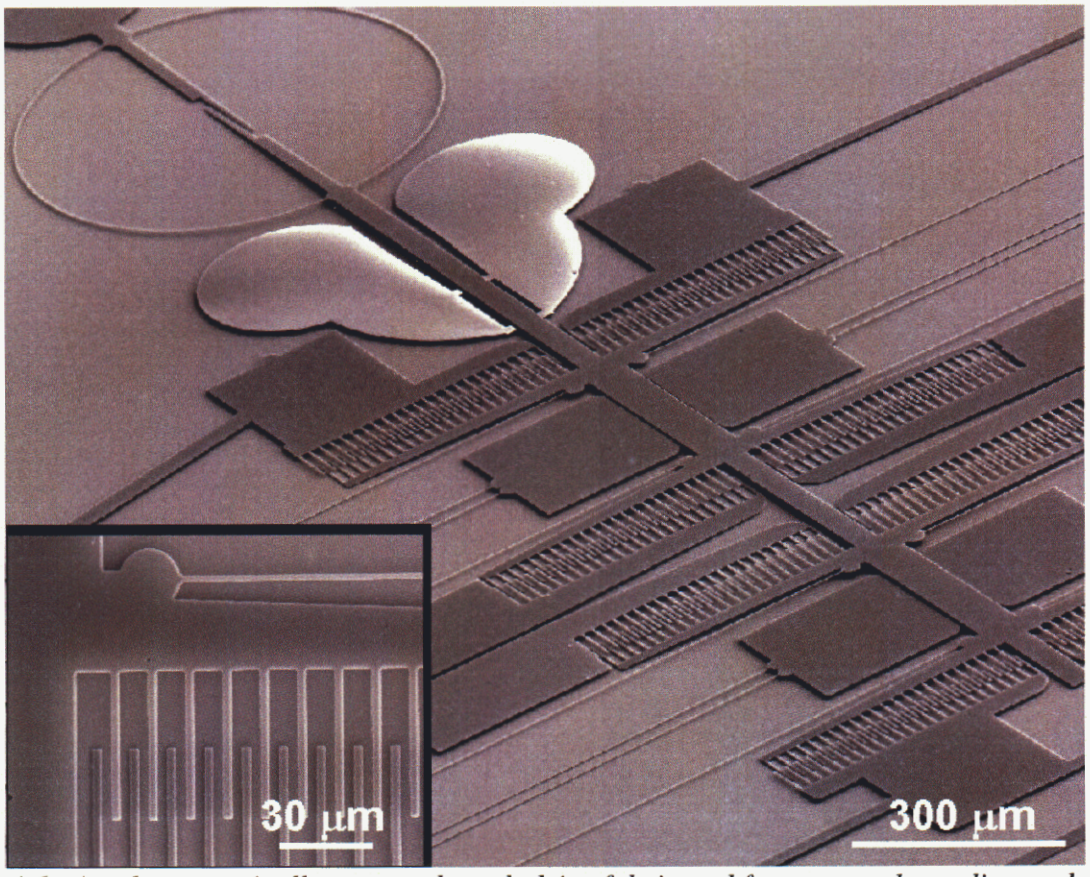

Fig. 4.6. An electrostatically-actuated comb drive fabricated from amorphous diamond. The inset shows detail of the amorphous diamond electrostatic fingers and spring.

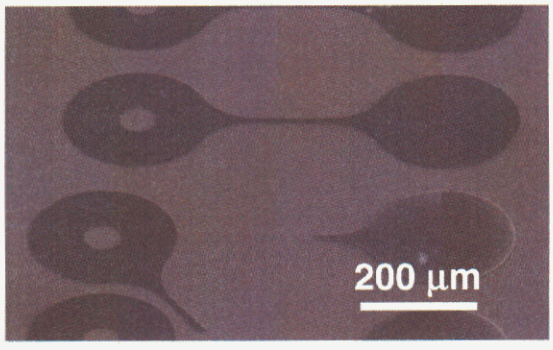

Fig 4.7. Micro-tensile test structures of aD.

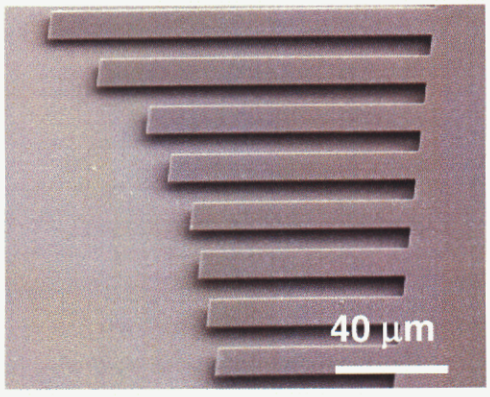

Fig. 4.8. aD cantilever beams.

Figures 4.7 and 4.8 show examples of micro-tensile test structures and cantilever beams of aD, respectively. The micro-tensile test structures permit measurement of the tensile stress-strain properties and tensile fracture strength and toughness of aD [29]. The cantilever beams are useful for measurement of the film bending modulus and assessment of strain gradients within the material. The control of strain gradients within a MEMS material is equally important as the control of the residual film stress. Strain gradients give rise to out-of-plane distortion of the MEMS structural element (even when the net residual stress is zero) and can prevent proper

meshing of gears or other, more serious, alignment errors. An example of an aD MEMS element with high residual strain gradient is shown in figure 4.9. Ideally, the radius of curvature of a MEMS beam should approach or exceed one meter (this radius of curvature would cause a 100 μm long beam to deflect about 50 Å out of the film plane). In most cases, proper control of film deposition and annealing leads to very little strain gradient in aD films (figures 4.6 - 4.8), but even in conditions where the strain gradient was not properly controlled in the as-fabricated structure (figure 4.9), the strain gradient can be subsequently corrected either by thermal annealing or post-deposition, see figures 4.10 (a) and (b), respectively.

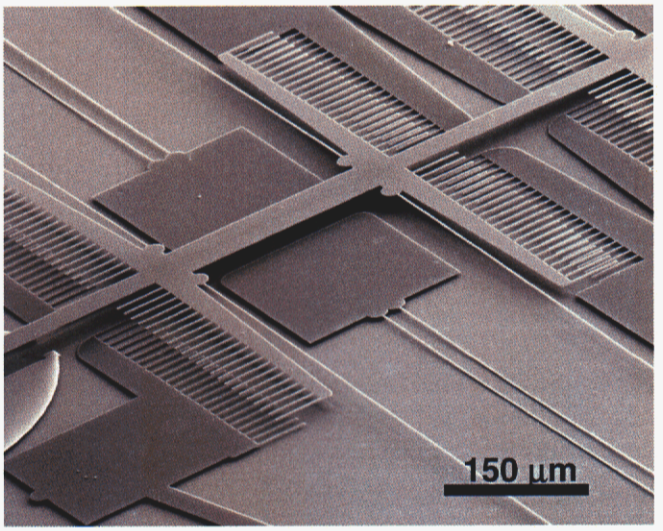

Fig. 4.9. Example of an aD MEMS structure in which the film has excessive negative strain gradient.

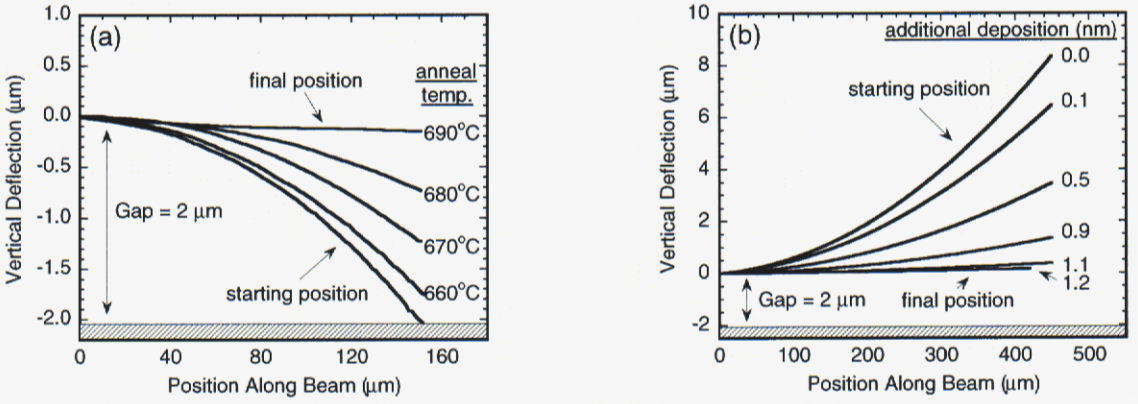

Fig 4.10. Control of the strain gradient in aD MEMS structures by (a) use of post-deposition annealing (5 min. at the indicated temperature) to eliminate negative strain gradient and (b) additional deposition (up to a total thickness indicated on plot) of compressively stressed carbon to eliminate positive strain gradient.

Figure 4.10(a) shows the result of post-MEMS fabrication annealing on an aD cantilever beam that exhibited high negative strain gradient (the beam height profile was measured by optical interferometry). Annealing at progressively higher temperatures (or longer times) at temperatures higher than the initial stress-relief temperature can reverse the strain gradient in aD films with negative curvature. If the initial strain gradient is in a positive direction, figure 4.10(b), the strain gradient can be reduced to near zero by post-deposition of compressively-stressed aD atop the MEMS structure. For the example shown in figure 4.10(b), the deposition of 1.2 nm of compressively-stressed aD is sufficient to increase the radius of curvature of the cantilever beam to 1.5 m.

4.3 Characterization of aD MEMS

The MEMS structures themselves prove to be particularly valuable for assessing the mechanical properties of aD, particularly because there is no bulk analog to aD in nature, and, therefore, it can not be tested using conventional approaches developed for bulk samples. We have used aD MEMS to determine a number of materials parameters, including elastic modulus, strength and fracture toughness, adhesion energy, etc. In addition, the surface of aD was found to be hydrophobic (with advancing H_2O contact angle of 85° to 95°), allowing easy release of the MEMS structures by a simple dehydration bake to drive off moisture. One of the areas of greatest interest in diamond and the hard amorphous carbons is in their expected excellent wear resistance which could enhance the lifetime of MEMS that have wear surfaces [30]. Using a MEMS-based friction and wear test structure that we have fabricated in aD, the performance of this material can be evaluated under realistic geometries, loads, and test frequencies that are found in an actual MEMS device [12].

The mechanical properties of aD are conveniently measured using micro-tensile test structures (Fig. 4.11). A nanoindenter tip is used to engage the ring end of the structure while the other end is firmly attached to the substrate by a pedestal of SiO_2. By measuring the lateral force and lateral displacement on the nanoindenter tip, a complete tensile stress-strain curve up to the point of fracture is obtained for the element [29]. Based on a large number of samples, the average elastic modulus of aD was found to be 830 (± 90) GPa (using bending modulus measurements from cantilever beams, the elastic modulus was found to be closer to 650 GPa) with a mean fracture strength of 8.5 (± 1.4) GPa [29]. All of the samples with the highest fracture strength appeared to have a surface flaw initiation site, while some samples with lower fracture strength had a readily-identifiable flaw within the gage section of the beam, see Fig. 4.12. Based on measurements where there was a readily-identifiable initial flaw or through measurement of the radius of the mirror-mist boundary on the fracture surface, the fracture toughness of aD was determined to be 8 $MPa \cdot m^{1/2}$ (about 8 times higher than poly-Si) [31].

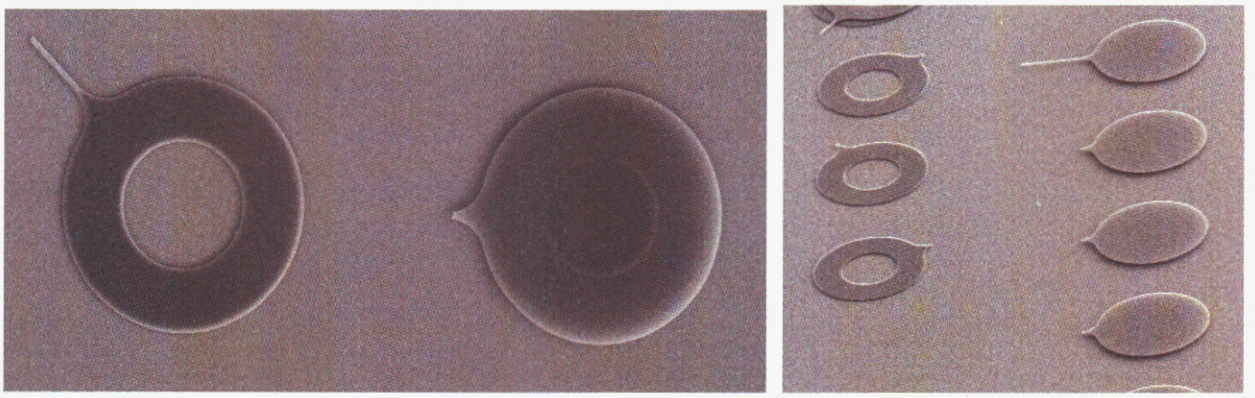

Fig. 4.11. Top and perspective views of aD pull-tab structures (the hole in the ring is ~50 μm diameter).

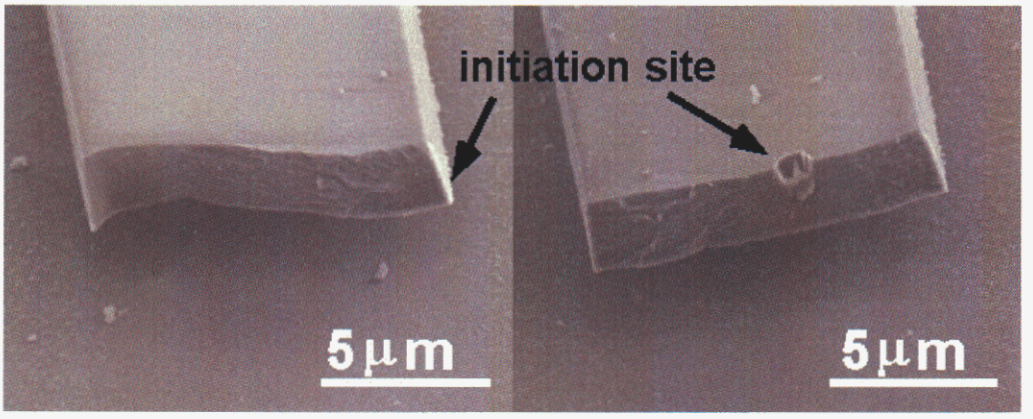

Fig 4.12. View of the fracture surfaces of two aD micro-tensile test specimens. In the specimen on the left, fracture originated on the sidewall of the beam. For the specimen on the right (which exhibited lower fracture strength) fracture originated at a bulk flaw.

Beam-bending measurements provide a more accurate means of determining the Young's modulus of aD. For these experiments, the deflection of a cantilever beam is measured interferometrically, as an electrostatic force is applied between the beam and ground. The electrostatic force provides a known load to the beam, while the deflection is easily measured to within 10's of nm. Electromechanical modeling is then used to account for the effect of the support compliance and non-zero take-off angle where the cantilever attaches to the support post, enabling accurate fitting of the force-deflection curve for the cantilever beam. An example of this measurement is shown in Fig. 4.13. From this data, a Young's modulus close to 650 GPa was found for aD.

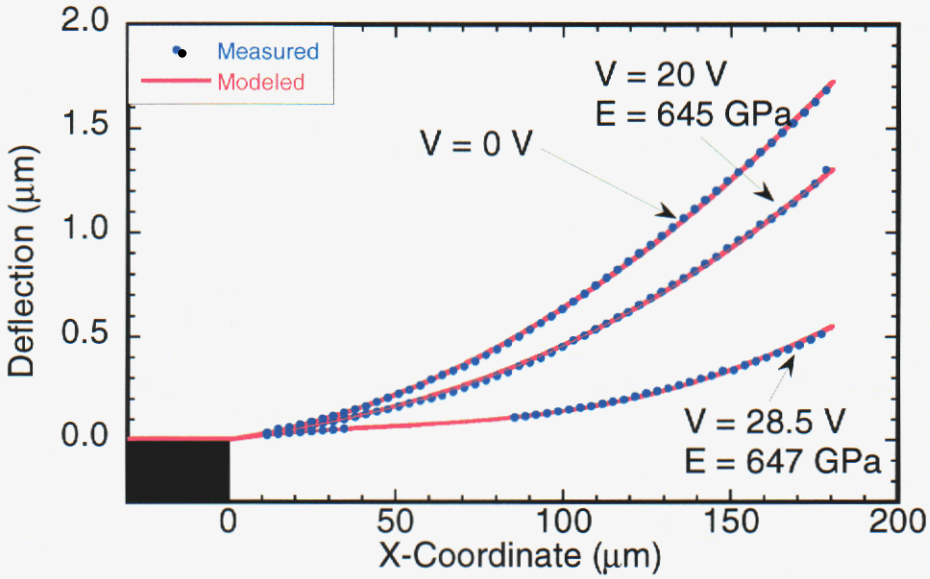

Fig. 4.13. Beam-bending measurement of the Young's modulus of aD. Electrostatic force is applied to a cantilever, and the beam deflection is measured interferometrically. Modeling of the force-deflection curves enables determination of the modulus, which is close to 650 GPa.

Most poly-Si MEMS structures are not limited by the material's mechanical properties, but the *chemical* properties of poly-Si can be limiting. Stiction or auto-adhesion of MEMS structures due to H_2O capillary forces is one example [11]. This stiction is due to the presence of the hydrophilic SiO_2 layer that is naturally-occurring on Si.. While there are established treatments to apply hydrophobic surface layers on the oxide surface, such as self-assembled monolayer coatings of octadecyltrichlorosilane [11], these coatings may not remain intact when their surfaces are in rubbing contact [30]. In contrast to Si surfaces, the surface of diamond tends to be hydrogen-terminated and relatively non-polar. Measurements of the advancing and receding H_2O contact angle on the surface of aD is shown in Table I for films in the as-stress-relieved and post-annealed state. The aD films are hydrophobic or nearly hydrophobic, contact angle 90° or larger, based on the static advancing contact angle numbers (the origin of the large hysteresis between static advancing and receding contact angles is not understood). It is believed that the increase in contact angle with annealing is due to desorption of oxygen from the carbon surface leaving a mostly hydrogen-terminated surface. The intrinsic high contact angles found for this material are especially useful for reducing stiction (contact adhesion) in MEMS structures, and this has been reflected in the ability to release the aD MEMS structures without the use of applied hydrophobic coatings or supercritical drying. Experimentally, we have found that a simple dehydration bake to drive off moisture is sufficient to release most structures, and, once released, there is no tendency for structures to re-adhere to the substrate when they are forced into contact.

Table I. *H_2O contact angles for as-stress-relieved and post-annealed aD.*

Material	Static advancing angle	Static receding angle
as-stress-relieved aD (600°C annealed)	84° ± 2°	57° ± 2°
850°C annealed aD	94° ± 2°	69° ± 2°

The adhesion energy between aD and Si was quantified through the measurements of long aD cantilevers that were exposed to 100% relative humidity for 24 hours. Under these conditions, long beams become stuck to the substrate due to capillary adhesion, see the schematic in Fig. 4.14. The adhesion energy is determined from the balance of the capillary adhesion force and the elastic restoring force of the bent cantilever beam, $\Gamma = \frac{3}{2} E \frac{h^2 t^3}{s^4}$, where Γ is the adhesion energy, E is the Young's modulus, and h, t, and s are defined in Fig. 4.14. From these measurements, we find that the adhesion energy between aD and Si is about 6 $\mu J/m^2$. For comparison, the adhesion between Si and Si is ~ 500 $\mu J/m^2$, nearly 100 times larger. It is expected that the adhesion between aD and aD would be even less than the 6 $\mu J/m^2$ value, but this has not yet been measured.

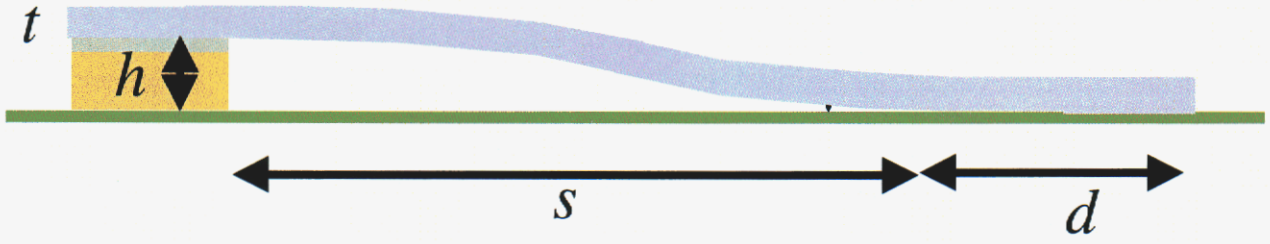

Fig. 4.14. Schematic of the geometry used for the measurement of the adhesion energy between aD and Si. Capillary force which causes a cantilever to remain in contact with the substrate is balanced by the elastic restoring force of the cantilever beam.

One factor that affects the adhesion energy between surfaces is the surface roughness. A very slight amount of surface roughness can be beneficial for limiting the contact area when surfaces are brought into contact, but rough surfaces are very undesirable. High roughness inhibits the ability to pattern a material with precision (structures with micron dimension can only be patterned if the surface roughness is less than a few 10's of nm). It also hinders the ability to create multi-level MEMS structures.

Measurements of the surface roughness on top of the aD MEMS structures using atomic force microscopy (AFM) reveal the surface to be very smooth (particularly when compared to CVD diamond surfaces), see figure 4.15. The very low surface roughness is due to the subplantation growth process (the high energy carbon ions implant below the surface, and their low mobility does not permit migration and rearrangement). As a result, the surface roughness of aD films replicates the surface roughness of the starting substrate. For films deposited on SiO_2, the surface roughness was measured to be 0.9 nm R.M.S. (figure 4.15), while films deposited directly on polished Si had a measured surface roughness of 0.1 nm R.M.S.

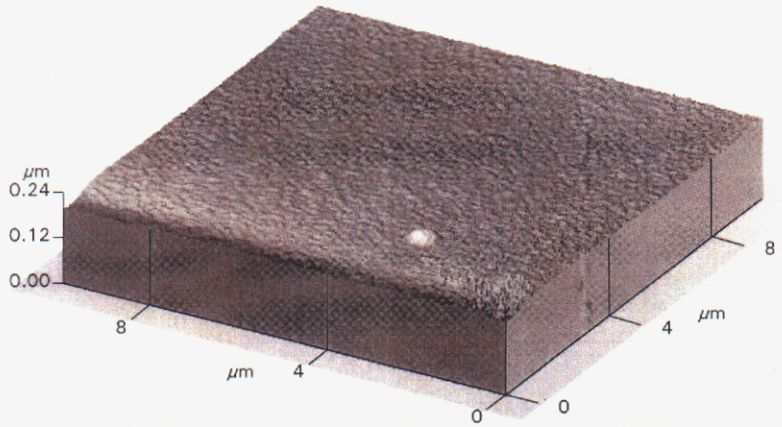

Fig. 4.15. AFM scan of the surface of an aD MEMS structure on SiO_2 on Si. The measured R.M.S. roughness was 0.9 nm.

One of the greatest expected advantages of aD for MEMS is its extreme wear resistance, and this is especially important for MEMS structures that have rubbing surfaces. (Wear has been found to be a concern for poly-Si MEMS, for example [30].) Conventional pin-on-disk wear tests of planar aD films have shown exceptionally low wear rates (no wear tracks identifiable using steel pins – tests using aD-coated pins are in preparation) and a low coefficient of friction, 0.1. Based on a design by Dugger *et al.* [32], a friction and wear MEMS test structure has been fabricated out of aD to allow wear evaluation under realistic loads, displacements, and frequencies found in typical MEMS devices, see Fig. 4.16. The initial friction and wear test structures suffered from problems due to charging of the Si_3N_4 layer beneath the MEMS (this charging causes electrostatic adhesion of the MEMS structures to the substrate). New structures are being processed, and results from these test structures are expected to be available in the near future.

The suite of properties for aD (controllable film stress and strain gradient, high strength, stiction-resistance, low wear) suggests it shows promise for supplementing poly-Si MEMS, particularly in applications where wear or stiction might be a concern. The greatest limitations with the material, however, lies in the lack of commercially-available deposition tools that can be readily inserted into an existing conventional Si microelectronics fabrication facility and in the fact that the deposition process itself is line-of-sight. Line-of-sight deposition prevents deposition on the undersides of surfaces or where there are re-entrant structures. The same design rules that apply to a multi-level poly-Si MEMS process do not apply for aD. These design rules have to be modified to employ features such as sloped oxide sidewalls for layers beyond the first structural layer. The fabrication of multi-level aD MEMS structures as well as hybrid poly-Si/aD MEMS are currently in development.

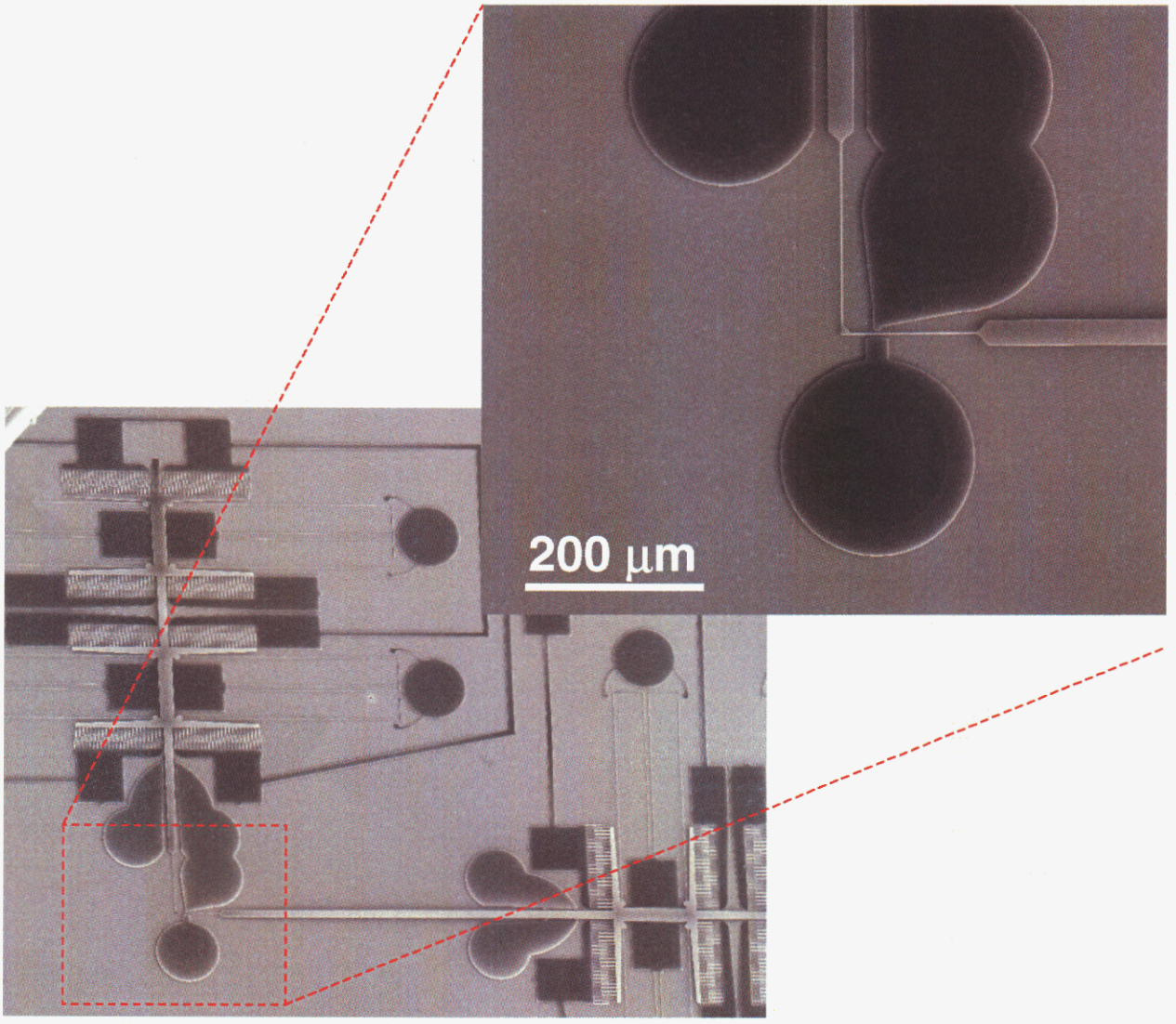

Fig. 4.16. A friction and wear MEMS test structure that is designed to test the coefficient of friction and wear properties of aD in a MEMS environment.

4.4 Conclusions and Future Directions

aD is potentially a quite useful new material for surface micromachined MEMS. It exhibits controllable stress and strain gradient, is stiction-resistant (due to a near-hydrophobic surface), has high strength and fracture toughness, has high modulus (which is desirable for mechanically-driven RF devices), is very smooth, and is expected to exhibit extreme wear resistance in MEMS applications. Proof-of-principle aD MEMS structures have been demonstrated (single level electrostatically-actuated comb drives and simple mechanical structures) and work is continuing on more advanced devices.

One of the immediate next generation aD devices are two-level aD MEMS structures. The key for producing these structures is the development of an alternative sacrificial layer to SiO_2 which can be deposited in Sandia's Compound Semiconductor Research Laboratory. Our

current development work is focusing on films of amorphous or polycrystalline Si that are wet etched using dilute HF in HNO_3. Using these sacrificial layers, two-level aD MEMS structures that are designed for the measurement of surface adhesion have been fabricated and chemically released. More advanced multi-level aD MEMS structures, including MEMS with captured hubs for rotating gears, are also being planned. An example of two of these multi-level hub designs is shown in Fig. 4.17. These multi-level structures will form the basic building blocks for advanced aD MEMS structures that demonstrate driven gears and complex motion.

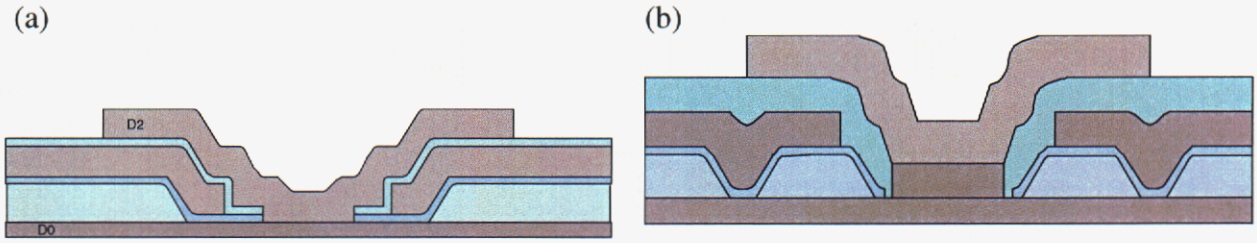

Fig. 4.17 (a) and (b). Two designs for a multi-level aD MEMS hub structure (aD layers in gray, sacrificial oxide layers in blue-green).

The development of aD MEMS has generated much popular press for Sandia. The work has appeared in Business Week, Popular Science and many other publications; it has been the subject of over five invited presentations at international conferences; and there is active interest in licensing this technology from Sandia. This work has also led to new, funded programs in the areas of implantable aD bioMEMS and the development of aD rf switches and nanoelectromechanical oscillators for rf signal processing. Rf electrical systems are an important technology for defense programs and communications.

5.0 Amorphous Diamond Sensors

5.1 Design of the FPW Sensor

In the area of sensors, increased sensitivity and functionality are key objectives. In this project, magnetically-excited flexural plate wave (FPW) sensors were developed using thin membranes of aD. The FPW device consists of a thin membrane that is supported at its edges by a thick substrate. Metal meander lines are patterned on top of the membrane, and an AC current is passed through the lines in the presence of a magnetic field in the film plane, see Fig. 5.1. The Lorentz force acting upon the metal lines alternately exerts an upwards or downwards force on the metal lines which acts to excite a plate wave in the membrane with periodicity equal to the meander line spacing. The resonant frequency of this plate wave is given by $\omega_{mn} = k_{mn}\left(\frac{Dk_{mn}^2 + T}{\rho_s}\right)^{1/2}$, where ω_{mn} is the resonant frequency for a membrane driven with wave vector, $k_{mn} = (m\pi/l, n\pi/w)$, D is the membrane bending moment = $E_Y t^3/[12(1-\nu^2)]$, T is the membrane tension, and ρ_s is the membrane mass areal density [33]. Increased sensitivity ($d\omega/d\rho_s$) is obtained by lowering the membrane mass, which is achieved by making the membrane as thin as possible. In order to operate the FPW device as a chemical sensor, a coating is applied to the membrane that is tuned to absorb the chemical of interest. Absorption

of the desired chemical into the coating causes a change in the mass of the coating, which leads to a shift in the resonant frequency of the plate wave. By tracking the shift in resonant frequency, the amount of absorption and, hence, the concentration of the chemical in the environment can be determined.

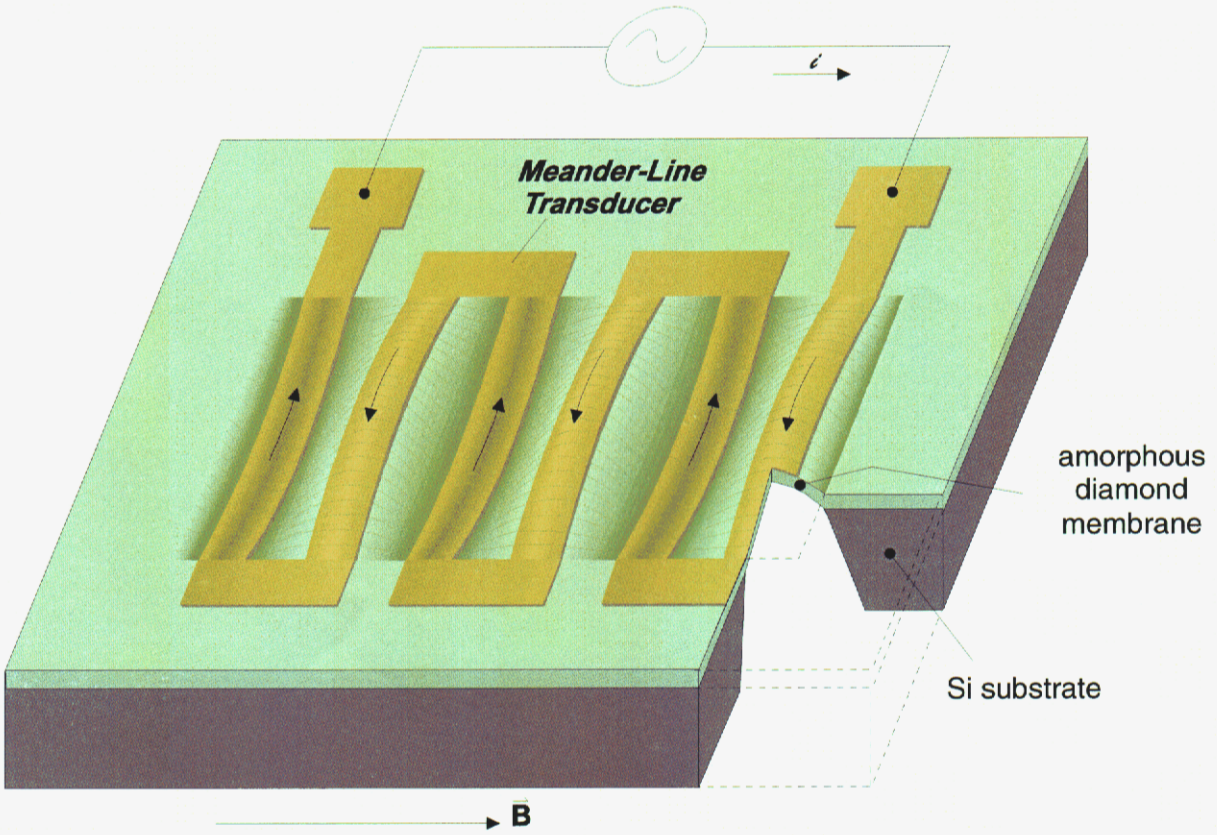

Fig. 5.1. Schematic of the FPW device.

5.2 Sensor Fabrication

In order to fabricate the aD FPW devices, it was necessary to develop a process to reliably fabricate thin membranes in aD with accurate dimensions. This processing was achieved by using a deep reactive ion etch tool (a Bosch etcher). The processing steps include (1) depositing aD on to a Si substrate and performing a stress relief anneal to achieve a *tensile* film stress of ~ 10 MPa, (2) patterning Al lines on to the aD surface using a lift-off process, (3) performing a double-side alignment to align a photoresist-defined opening on the backside of the wafer with the patterned Al lines on the front of the wafer, and (4) performing a deep reactive ion etch from the backside of the wafer to define the membrane. These steps are illustrated in Fig. 5.2. One of the significant advantages of aD for FPW device fabrication is that the chemistry for deep reactive ion etching of Si is very selective for Si. Our measurements indicate that the Si etch rate exceeds the aD etch rate by more than 1000 to 1. This permits additional process flexibility, i.e. the etch time can be extended to ensure adequate removal of all Si from the membrane openings without causing significant etching of the aD within the membrane openings.

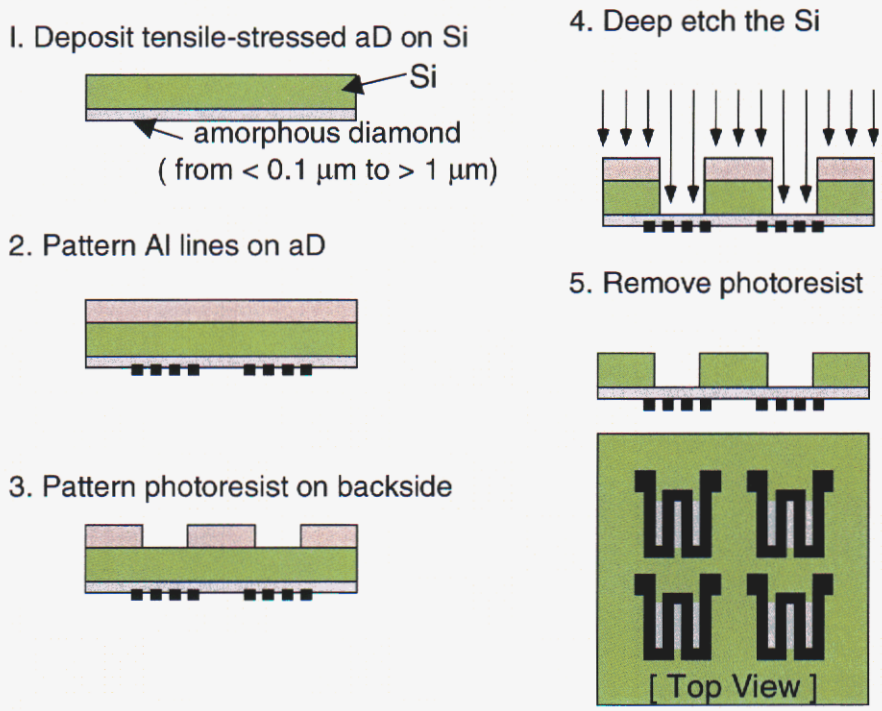

Fig. 5.2. Processing steps to create an aD FPW device.

Fig. 5.3. shows a close-up of one of the aD FPW devices as well as an array of devices fabricated from an aD-coated 4" wafer (the deposition process for aD produces a 3" by 3" *square* region that has uniform thickness and properties in the center of the 4" wafer). By varying the sizes of the membranes in the array and the spacing and number of metal transducer lines, the resonant frequency of the FPW devices can be changed. The thickness of the aD was also varied, from about 0.08 μm to > 1 μm, in order to determine the effect of membrane mass on device sensitivity and performance.

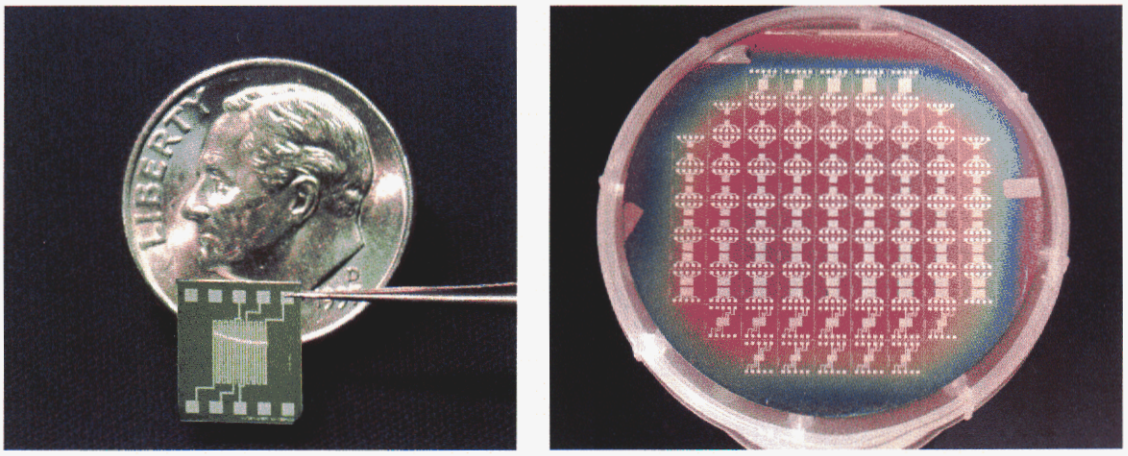

Fig. 5.3. A close-up view of an aD FPW device and an array of aD FPW devices fabricated from a single 4" wafer.

5.3 Sensor Characterization

The operation of the aD FPW device can be tested by measurement of the coupling efficiency between two transducer lines patterned on to the aD surface. There are two modes of operation: the transducers may be measured independently by looking at the impedance vs. frequency for each line (the impedance fluctuates due to the induced voltage created when a current carrying line moves in the magnetic field), or a transmission measurement may be performed in which one line is driven with an AC current and the other transducer line is used to detect the magnitude of the induced signal. Fig. 5.4 shows the results of these types of measurements for an aD FPW device. An FPW device with good performance will show similar response when the two transducers are operated independently, Fig. 5.4(a), or will show a sharp peak in the transmission spectrum, Fig. 5.4(b). The presence of multiple peaks in Fig. 5.4 is due to the excitation of plate waves with different wave vector. Finite element modeling has shown that for FPW devices that are designed for a 20,1 wave vector (meaning the resonance mode has 20 nodes in the x-direction and 1 node in the y-direction, which is determined by the pitch of the transducer lines patterned on the membrane), the 19,1 and 21,1 modes are also excited with reasonable intensity. This explains why there a few intense peaks that neighbor the dominant resonance peak, as shown in Fig. 5.4.

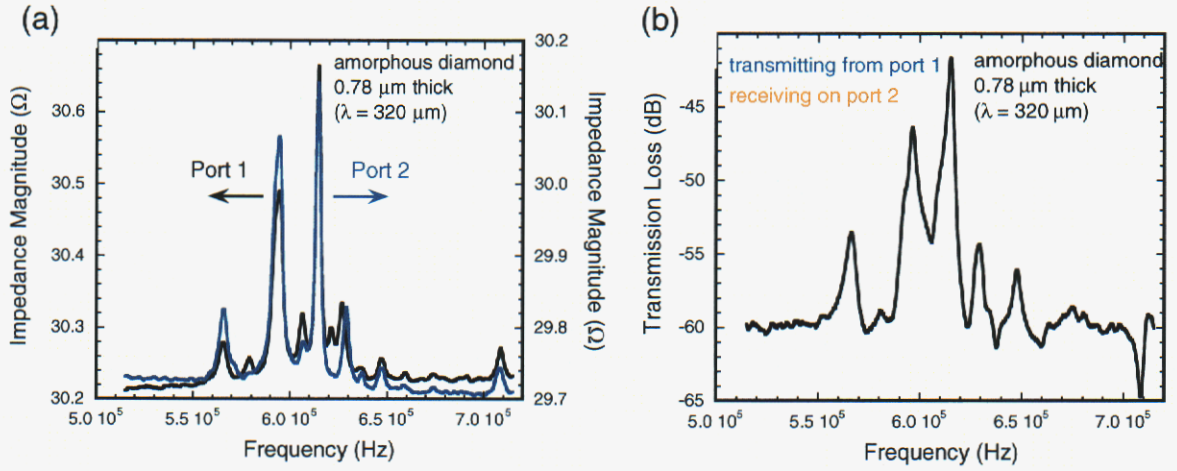

Fig. 5.4. Measured electrical characteristics of an aD FPW device. (a) Measured impedance vs. frequency for each set of transducer lines on a dual transducer (dual port) FPW device. (b) Measured transmission loss for coupling between a driven transducer to a receiving transducer. Narrow, intense peaks are indicative of good device performance.

In order to operate the FPW device as a chemical sensor, a coating is applied to the FPW device that is sensitive to the chemical of interest. For initial testing of the aD FPW devices as chemical sensors, a coating of ethyl cellulose was applied to the device using spray coating. An uncoated neighboring FPW device was used as a reference and control. The devices were tested with a variety of volatile organic compounds (VOCs), including methanol, acetone, methyl chloride, and chloroform, and good sensitivity was obtained. Fig. 5.5 shows the aD sensor response to chloroform, perchloroethylene, and xylene. The fabricated sensors showed good sensitivity to the VOCs down to the 2 ppm level with a net sensitivity a few times better than a

comparable Si_3N_4-based sensor. The greatest sensitivity (magnitude of frequency shift per concentration unit of solvent) was found for xylene, but the detector response was slower for this VOC than for chloroform. The specificity of the sensor and its response time is strongly dependent on the chemical sensing coating that is employed, however. A coating different than ethyl cellulose would be expected to give a different response. For detection of a specific chemical, optimization of a specific coating would need to be performed. An important point regarding sensor performance, however, is that the aD FPW sensor performed very well, compared to sensors that were developed using Si_3N_4 membranes. Even further sensitivity improvement is expected by reducing the aD membrane thickness from 0.37 μm to a thickness less than 0.1 μm. Modeling indicates that a factor of ~ 50 improvement over the 1 μm thick Si_3N_4 FPW sensors should be achievable for the < 0.1 μm thick aD FPW sensors. Development of these very high sensitivity FPW sensors is in progress.

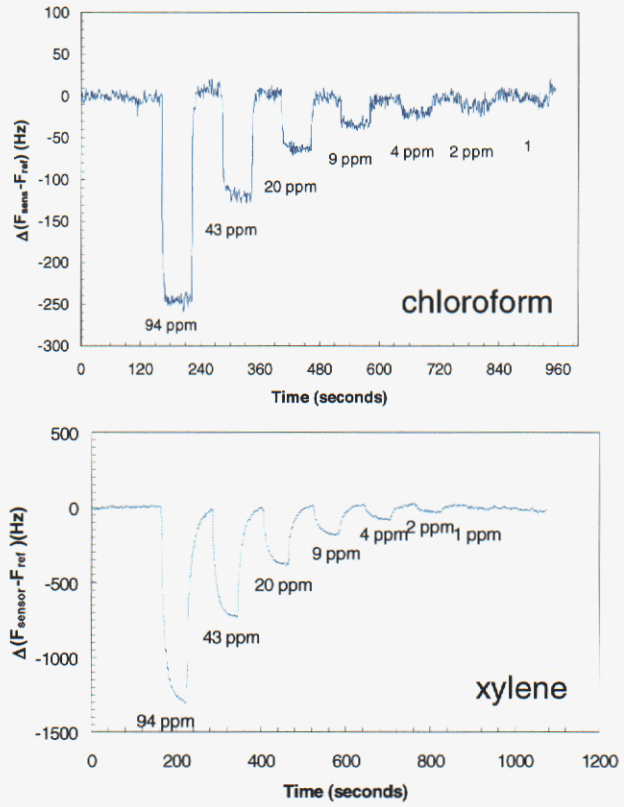

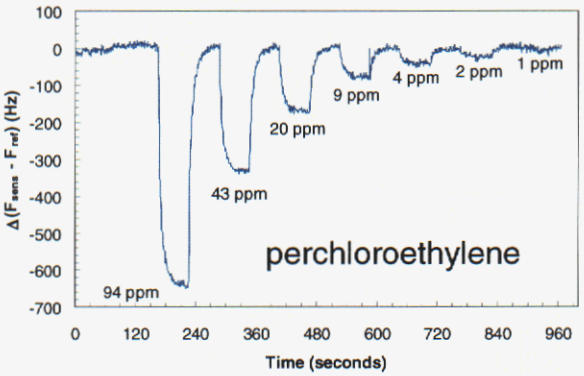

Fig. 5.5. Measured response of the aD FPW sensor to chloroform, perchloroethylene, and xylene when an ethyl cellulose coating is applied to the device. The most sensitive response was to xylene, and the fastest response was to chloroform.

5.4 Measurements Based on aD Membranes

aD membranes that were developed for the creation of FPW sensors have also been useful for the measurement of fundamental properties of aD. One example is the use of aD membranes for the measurement of optical absorption from the UV down to the IR wavelengths. Fig. 5.6. shows the optical absorption in a 1.1 μm thick aD membrane that was measured using photothermal deflection spectroscopy. The oscillations in the absorption coefficient are due to Fabry-Perot interference from light reflected off of the front and back surfaces of the membrane. From the periodicity of the oscillations, the refractive index of the aD film is estimated to be 2.4.

aD films show anomalously high optical absorption in the visible and IR wavelengths when compared to crystalline diamond films. This high optical absorption is due to optical absorption within the π-bonded 3-fold clusters in the material. From the optical absorption measurements, a determination of the distribution of 3-fold one-dimensional cluster sizes (i.e. chain sizes) can be obtained using our model of this material's electronic density of states, see right panel of Fig. 5.6.

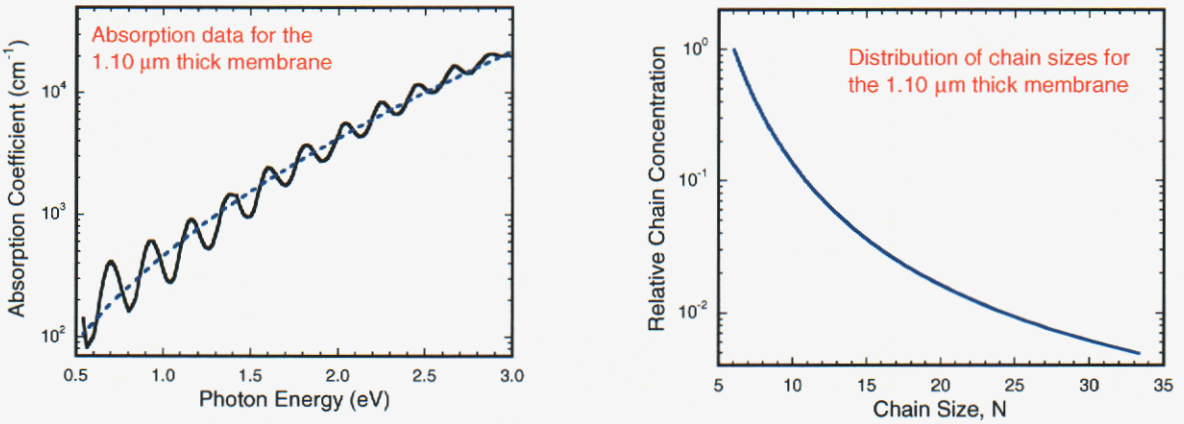

Fig. 5.6. (left) Measured optical absorption in aD, and (right) derived distribution of one-dimensional 3-fold carbon cluster sizes in this film.

Mechanical property information can also be obtained from aD membranes. One approach is the use of bulge testing to measure the elastic modulus and residual stress in aD membranes. Fig. 5.7 shows the measured pressure-deflection curves for a 6 mm diameter, 427 nm thick aD membrane. The pressure divided by the maximum deflection, d, is linearly proportional to the residual stress and Young's modulus, $\frac{P}{d} = \frac{4t}{a^2}\sigma_0 + \frac{8t}{3a^4}\frac{E_Y}{(1-\nu)}d^2$, where t is the membrane thickness, a is the membrane diameter, σ_0 is the residual stress, and ν is the Poisson ratio. For this membrane, the measured Young's modulus is ~ 650 GPa and the residual tensile stress is ~ 140 MPa, see right panel of Fig. 5.7. The measured value of Young's modulus is in good agreement with the value obtained from beam bending measurements.

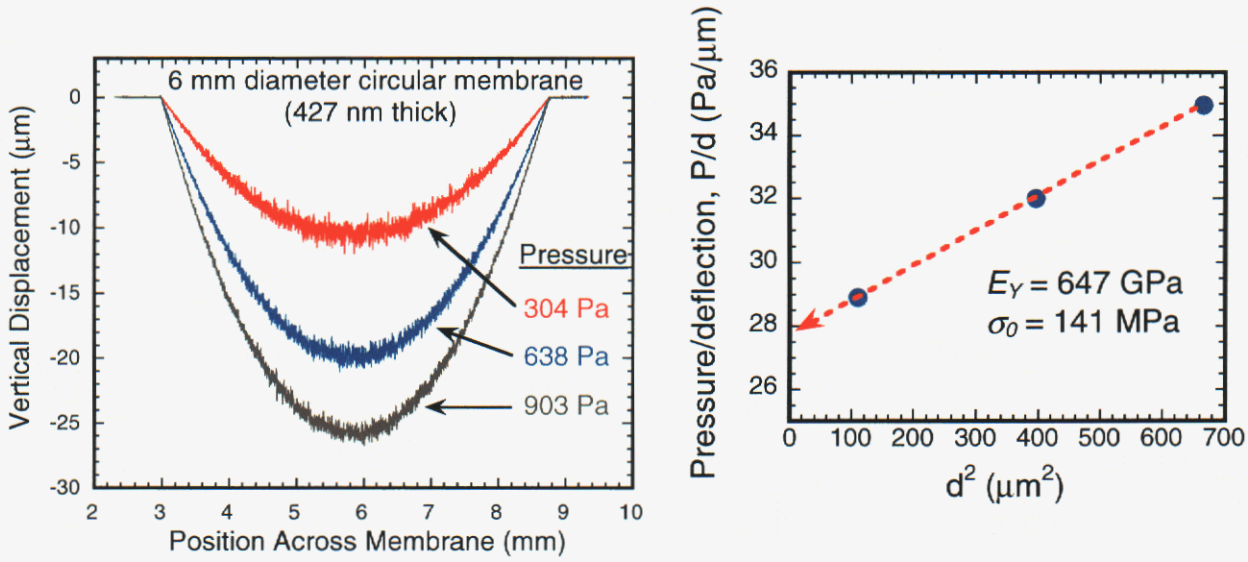

Fig. 5.7. (left) Measured pressure-deflection curves for a 6 mm diameter, 427 nm thick aD membrane, and (right) P/d vs d^2 plot used to determine the Young's modulus, E_Y, and residual tensile stress, σ_0.

6. 0 Summary: Impact and Future Directions of aD on MEMS and Sensors

aD has a combination of properties not found in any other material. These mechanical properties include hardness and stiffness second only to the crystalline diamond. In addition, the material has the unusual property that it can undergo an internal structural rearrangement that permits the material to relieve its internal stress at modest temperatures while at the same time maintaining its property of being extremely hard.

Micromachines fabricated from aD are very hard and durable. Mechanically, the components of these machines (linkages, gears, etc.) have properties like that of crystalline diamond which is distinguished by its extraordinary wear resistance. Another important property of aD is that the material is bio-compatible (it does not degrade in the body, nor does it provoke a negative response by tissues in the body). This material's property is not possessed by silicon and, thus, aD MEMS may be one approach for the creation of machines or sensors that could be implanted into the human body (e.g. bioMEMS). Initial bio-compatibility testing of aD was performed in order to evaluate the viability of aD bioMEMS structures. Endothelial capillary cells were grown on uncoated and fibronectin-coated aD surfaces, and it was observed that there was abundant cell growth and adhesion on the fibronectin-coated surface, but little adhesion to the uncoated surface. This result indicates that aD MEMS would be especially valuable as bioMEMS, and this could be important for future Sandia programs.

The sensors developed from the amorphous diamond similarly benefit from this material's exotic properties. Because of the inherent strength of this material and the ability to control the materials stress, it is possible to create membranes of this material that are very thin, yet sufficiently durable. This enables the creation of high-sensitivity membrane-based sensors.

Many companies have commercialized or are commercializing a variety of MEMS and sensors technologies, including: Texas Instruments, Analog Devices, Lucent Technologies, Hewlett Packard, IBM, Honeywell. There are also a large number of universities with active research programs, including: MIT, Stanford, UC Berkeley, Univ. Wisconsin, and Case Western Reserve Univ. In contrast to the efforts occurring at all of these companies and universities, our technology is the only one that uses aD for the fabrication of MEMS and sensors, setting this Sandia technology apart from competing technologies that rely almost exclusively on silicon, silicon nitride, silicon carbide, or metals such as nickel or tungsten.

There is considerable commercial interest in MEMS and microsensors because of their potential impact on all segments of society from telecommunications to medical/biochemical applications to environmental enhancement. To date, the overwhelming majority of these microsystems are made from silicon. R.H. Grace (Sensors Magazine, July 2000) recently wrote, "the major growth in the MEMS market will be in the arena of new MEMS: devices that will enable such killer applications as extremely high volume telecommunications and biomedical innovations." In order to make many new "killer applications" happen, it will likely be necessary to expand the MEMS-material base to include new materials, such as aD. aD has been proven to be compatible with silicon and silicon MEMS processing, and this opens up the possibility of creating hybrid MEMS structures that would employ poly-Si MEMS for much of the device and use aD in certain critical areas, such as areas of rubbing contact. We have already demonstrated some multi-level aD MEMS designs with a hybrid structure. These structures consisted of patterned poly-Si combined with aD structural elements – spring-supported resonating plates – and were developed to enable acoustic sensing using small MEMS structures.

This project on the fabrication of aD MEMS and sensors has led to a number of fruitful outside collaborations. For example, NASA is using some of Sandia's aD films as collectors of solar wind particles for the Genesis space mission that launched in 2001. The stress-free aD films were especially suited for this application since they can be grown not only thick but with extremely low impurity levels (e.g. less than 2 ppm of hydrogen) which is critical for analysis of the composition of the solar wind. This collaboration has driven us to develop large area growth and processing of aD films, a necessary component for successful commercialization of this technology. Free-standing membranes of aD have also been provided to several research groups for evaluation as x-ray or electron transparent windows. Thin aD membranes are very robust and, because carbon is a low Z material, they are uniquely suited for masks in next generation electron or x-ray lithography tools (the development of which is crucial to the future advancement of the microelectronics industry).

7.0 Acknowledgments

The authors would like to thank Charles Barbour for technical oversight and contributions to this project, Peter Schultz for density functional theory of aD, Xidong Chen for fluctuation microscopy, Todd Alam for solid state NMR, Klas Hjort and Orlando Auciello for input on polycrystalline and nanocrystalline diamond films, Mary-Anne Mitchell for aD MEMS and FPW sensor processing, Bonnie McKenzie for SEM imaging, John Hunter for AFM imaging, Tom Buchheit and Jill Glass for thin film mechanical testing and fracture mechanics, Brian Jensen for modeling and analysis of beam deflection, Bruce Bunker and Jim Kushmerick

for H_2O contact angle measurements, Mike Dugger for friction and wear test structure design and measurement, and Carl Seager for photothermal deflection spectroscopy measurements.

8.0 References

[1] N. A. Marks, D. R. McKenzie, B. A. Pailthorpe, M. Bernasconi, and M. Parrinello, Phys. Rev. Lett. **76**, 768 (1996); Th. Frauenheim, G. Jungnickel, Th. Köhler, P. Stitch, and P. Blaudeck, Proc. 1st Int. Meeting on Amorphous Carbon (World Scientific Publ., Singapore, 1998).

[2] P. A. Schultz, K. Leung, and E. B. Stechel, Phys. Rev. B **59**, 733 (1999).

[3] T. A. Friedmann, J. P. Sullivan, J. A. Knapp, D. R. Tallant, D. M. Follstaedt, D. L. Medlin, and P. B. Mirkarimi, Appl. Phys. Lett. **71**, 3820 (1997).

[4] J. P. Sullivan, T. A. Friedmann, and A. G. Baca, J. Electron. Mater. **26**, 1021 (1997).

[5] X. Chen, J. M. Gibson, J. Sullivan, T. Friedmann, and P. Volyes, Mater. Res. Proc. **638**, F14.40.1 (2001).

[6] J. M. Gibson and M. M. J. Treacy, Phys. Rev. Lett. **78**, 1074 (1997); M. M. J. Treacy, J. M. Gibson, P. J. Keblinski, J. Non-Cryst. Sol. **231**, 99 (1998).

[7] T. A. Friedmann, K. F. McCarty, J. C. Barbour, M. P. Siegal, and D. C. Dibble, Appl. Phys. Lett. **68**, 1643 (1995).

[8] J. P. Sullivan, T. A. Friedmann, R. G. Dunn, E. B. Stechel, P. A. Schultz, M. P. Siegal, and N. Missert, Covalently Bonded Disordered Thin Film Materials, (Mater. Res. Soc. Symp. Proc. 498, Warrendale, PA 1998) p. 97.

[9] J. Robertson, Adv. Phys. **35**, 317 (1986).

[10] M. N. Gardos, in Tribology Issues and Opportunities in MEMS, edited by B. Bhushan (Kluwer Academic Publishers, Netherlands, 1998) p. 341.

[11] R. Maboudian and R. T. Howe, J. Vac. Sci. Technol. B **15**, 1 (1997).

[12] J. P. Sullivan, T. A. Friedmann, M. P. de Boer, D. A. LaVan, R. J. Hohlfelder, C. I. H. Ashby, M. T. Dugger, M. Mitchell, R. G. Dunn, and A. J. Magerkurth, in Materials Science of Microelectromechanical Systems (MEMS) Devices III, edited by M. P. de Boer, M. Judy, H. Kahn, and S. M. Spearing (Mater. Res. Soc. Symp. Proc. 657, Warrendale, PA, 2001).

[13] H. Björkman, P. Rangsten, P. Hollman, and K. Hjort, Sensors and Actuators **73**, 24 (1999).

[14] H. Björkman, P. Rangsten, and K. Hjort, Sensors and Actuators **78**, 41 (1999).

[15] E. Kohn, P. Gluche, and M. Adamschik, Diamond Relat. Mater. **8**, 934 (1999).

[16] S. Ertl, M. Adamschik, P. Schmid, P. Gluche, A. Flöter, and E. Kohn, Diamond Relat. Mater. **9**, 970 (2000).

[17] T. Shibata, Y. Kitamoto, K. Unno, and E. Makino, J. Microelectromech. Systems **9**, 47 (2000).

[18] R. Ramesham, Thin Solid Films **340**, 1 (1999).

[19] O. Auciello, A. R. Krauss, D. M. Gruen, H. G. Busman, E. M. Meyer, J. Tucek, A. Sumant, A. Jayatissa, N. Moldovan, D. C. Mancini, and M. N. Gardos, in Materials Science of Microelectromechanical Systems (MEMS) Devices II, edited by M. P. de Boer, A. H. Heuer, S. J. Jacobs, and E. Peeters (Mater. Res. Soc. Symp. Proc. 605, Warrendale, PA, 2000) p. 73.

[20] W. P. Kang, J. L. Davidsson, Q. Li, J. F. Xu, D. L. Kinser, and D. V. Kerns, Transducers '95 and Eurosensors IX, Stockholm, Sweden, June 25-29, 1995.
[21] W. Kulisch, A. Malave, G. Lippold, C. Mihalcea, and E. Oesterschulze, Diamond Relat. Mater. **6**, 906 (1997).
[22] M. Y. Mao, T. P. Wang, J. F. Xie, and W. Y. Wang, Proc. IEEE Micro Electro Mechanical Systems 1995, Amsterdam, Netherlands, p. 392.
[23] M. Aslam and D. Schulz, Transducers '95 and Eurosensors IX, Stockholm, Sweden, June 25-29, 1995.
[24] J. D. Hunn, S. P. Withrow, C. W. White, R. E. Clausing, and L. Heatherly, Appl. Phys. Lett. **65**, 3072 (1994).
[25] Ph. Niedermann, W. Hänni, N. Blanc, R. Christoph, and J. Burger, J. Vac. Sci. Technol. A **14**, 1233 (1996).
[26] V. S. Trava-Airoldi, E. J. Corat, E. Del Bosco, and N. F. Leite, Surf. Coatings Technol. **76-77**, 797 (1995).
[27] M. G. Jubber, A. J. McLaughlin, J. H. Marsh, J. S. Aitchison, P. John, C. E. Troupe, J. I. B. Wilson, Diamond Relat. Mater. 7, 1148 (1998).
[28] O. J. A. Schueller, S. T. Brittain, G. M. Whitesides, Sensors and Actuators A **72**, 125 (1999).
[29] D. A. LaVan, R. J. Hohlfelder, J. P. Sullivan, T. A. Friedmann, M. Mitchell, and C. I. H. Ashby, in Amorphous and Nanostructured Carbon, edited by J. P. Sullivan, J. Robertson, O. Zhou, T. B. Allen, and B. F. Coll (Mater. Res. Soc. Symp. Proc. 593, Warrendale, PA, 2000) p. 465.
[30] P. Weiss, Science News **158**, 56 (2000).
[31] T. A. Friedmann, J. P. Sullivan, D. A. LaVan, T. E. Buchheit, J. A. Knapp, R. J. Hohlfelder, and M. Mitchell, presented in *Symposium W: The Limits of Strength in Theory and Practice* (2000 Fall Meeting of the Mater. Res. Soc., Boston, MA, Nov. 27 - Dec. 1, 2000).
[32] M. T. Dugger, D. C. Senft and G. C. Nelson in Microstructure and Tribology of Polymer Surfaces, edited by V.V. Tsukruk and K.J. Wahl (American Chemical Society, Washington, DC, 1999), p. 455.
[33] S. J. Martin, M. A. Butler, J. J. Spates, M. A. Mitchell, W. K. Schubert, J. Appl. Phys. **83**, 4589 (1998).

APPENDIX I: Summary of Materials Properties of Amorphous Diamond

Property	Amorphous Diamond	Comment
Density, ρ	$2.9 \pm \sim 0.1$ g/cm^3	mostly based on x-ray reflectivity measurements
Hardness	80 GPa	based on nanoindentation with finite element modeling of the tip and sample
Elastic Modulus, E_Y	650 – 800 GPa	based on pure tensile test specimens and beam bending (the lower value was from beam bending)
Poisson's ratio, ν	~ 0.12	not measured by us; measurements are based on the value for diamond and surface Brillouin scattering measurements of similar carbon films
Tensile Strength	8 GPa	based on tensile test specimens
Fracture Toughness, K_{IC}	8 MPa·m^{½}	based on identification of flaw sizes and the features in the fracture surface following tensile fracture of beams
Film Stress	tunable from 8 GPa compressive to ~ 0.1 GPa tensile, typically about ± 50 MPa for MEMS structures	8 GPa is the as-deposited stress state which typically decreases with annealing (zero residual stress obtained after ~ 650°C annealing)
Strain gradient	tunable from about 10 mm positive radius of curvature to 10 mm negative radius of curvature negative (as measured on released cantilever beams)	tunability achieved by tailoring film stress of individual layers in a multi-layer film or by post-processing (e.g. annealing)
Coefficient of friction	~0.1 using a steel pin in air	standard pin-on-disk measurement

Wear resistance	~ 10,000 times better than Si	not measured by us; value is estimated based on work of M. N. Gardos that claimed crystalline diamond is 10,000 times more wear resistant than Si
Thermal stability	little change with annealing up to ~ 800°C in inert environment, ok up to about 400°C in an oxidizing environment (e.g. air)	there are some changes detectable by Raman spectroscopy, optical absorption, and electrical measurements below 800°C, but these seem to affect the mechanical properties only very little; the temperature limit in air is due to oxidation of the carbon
Thermal conductivity, κ	~ 1 $Wcm^{-1}K^{-1}$	not measured by us; this value is based on a reported value for a diamond-like carbon film (which was hydrogenated); the amorphous diamond films likely have a somewhat higher value
Coefficient of thermal expansion, α	~ 2 x 10^{-6} K^{-1}	value is based on measurement of the thermal mismatch stress for an amorphous diamond film on Si; Tom F. has data as a function of temperature
Specific heat, C_p	~ 0.6 $Jg^{-1}K^{-1}$ (at 300 K)	estimate using a rule of mixtures between diamond and graphite – probably ok within $\pm$ 0.1 $Jg^{-1}K^{-1}$
Electrical resistivity	tunable from ~ 0.1 Ωcm to 10^7 Ωcm – for MEMS structures, typically 10^4 Ωcm	the as-deposited electrical resistivity is high (10^7 Ωcm), and this drops with annealing; the in-plane resistivity for a MEMS structure is typically 10^4 Ωcm
Optical absorption	λ-dependent, from about 10^2 cm^{-1} at $h\nu$ = 0.5 eV, about $3x10^3$ cm^{-1} at $h\nu$ = 2 eV, and $2x10^4$ cm^{-1} at $h\nu$ = 3 eV	measurements are based on photothermal deflection spectroscopy using membranes of amorphous diamond
Refractive index, n	2.5 at $h\nu \approx 2$ eV	measurements are based on the Fabry-Perot oscillations observed in the absorption spectra

Thickness range	tunable from about 0.005 μm to about 8 μm	in principle, there is no upper or lower limit to thickness, and these values simply suggest realistic ranges
Deposition area	up to 4" diameter	the deposition rate scales with deposition area (the dep. rate over a 4" diameter substrate is ¼ the dep. rate over a 2" diameter substrate)
Deposition rate	1 μm in about 2 – 3 hours on a 2" diameter substrate	see note above; the thickness and properties are uniform in this area to within about 10% going from center to edge
Surface roughness	substrate dependent: 0.1 nm rms roughness for 1 μm film on Si, 1 nm rms roughness for 1 μm film on SiO_2 on Si (MEMS structure)	measurements are based on AFM
Contact angle with H_2O	84° for as-produced MEMS, 94° after annealing at 850°C	measurements are for advancing contact angles

APPENDIX II: Design Rules for Processing Amorphous Diamond for MEMS

1. The minimum feature size (for optical contact lithography) = 1 μm; minimum features of 2 μm print more reliably.

2. Long and thin structures up to 2 mm in length and a few μm in width can be released reasonably reliably.

3. Both curved and rectilinear structures print and develop fine. There is no known asymmetry in the properties of amorphous diamond, so the structures may be printed in arbitrary orientations on the wafer. [If the structures are to be aligned with KOH etch holes in the Si wafer, then alignment and orientation of the structures are important.]

4. Release holes should be > 2 μm x 2 μm, if possible.

5. Design the mask so that structures that are to remain attached to the substrate have a minimum dimension greater than the width of the widest structure that is to be fully released. Doubling this dimension is safer. For example, if the widest beams that are to be fully released are 20 μm wide, then the minimum width of the structures that are to remain attached needs to be at least 20 μm, with 40 μm being much safer. We typically design the structures that are to remain attached to the substrate to be as wide as the design and real estate allow so that timing of the release etch is less critical.

6. It is a good idea to design the mask so that one release etch time is ok for all of the structures on the mask. It is possible to do the release etch in steps so that, for example, tiny structures can be released and measured first, and then bigger structures can be released at a later date, but this is typically less desirable.

7. It is a good idea to make the electrical lines that feed the device wide enough so that they do not release from the substrate. If they do release, there is danger that they can warp and ground the MEMS structure to the substrate.

DISTRIBUTION:

5	MS 1421	J. P. Sullivan, 1112
1	MS 1415	J. C. Barbour, 1112
1	MS 1415	T. A. Friedmann, 1112
1	MS 1425	C. I. Ashby, 1744
1	MS 1081	M. P. de Boer, 1762
1	MS 0603	W. K. Schubert, 1763
1	MS 0603	R. J. Shul, 1763
1	MS 1179	R. J. Hohlfelder, 15341
1	MS 1079	Marion W. Scott, 1700
1	MS 1080	Jerome F. Jakubczak II, 1703
1	MS 1425	Stephen J. Martin, 1707
1	MS 0603	Charles T. Sullivan, 1742
1	MS 0918	Central Technical Files, 8945-1
2	MS 0899	Technical Library, 9616
1	MS 0612	Review and Approval Desk, 9612 for DOE/OSTI
2	MS 0188	Donna L. Chavez, LDRD Office, 1030